Article

Human brain organoids record the passage of time over multiple years

https://doi.org/10.1038/s41586-026-10877-x

Received: 2 July 2025

Accepted: 1 July 2026

Published online: 19 August 2026

Open access

Check for updates

Irene Faravelli[1,2,10,12], Noelia Antón-Bolaños[1,2,11,12], Anqi Wei[1,2], Tyler Faits[1,2], Abhishek Sampath Kumar[1,2], Sophia Andreadis[1,2], Rahel Kastli[1,2], Marta Montero Crespo[1,2], Mara Steiger[3,4], Daniel Leible[5], Elizabeth Zhang[5], Bobae An[5], Yaron Meirovitch[6], Sayara Silwal[1], Sung Min Yang[1,2], Alexander Kovacsovics[3], Xian Adiconis[2,7], Helene Kretzmer[3,4], Joshua Z. Levin[2,7], Edward S. Boyden[5], Jeff Lichtman[6], Aviv Regev[7,8], Alexander Meissner[3,9] & Paola Arlotta[1,2] ✉

The human brain develops and matures over an exceptionally prolonged period of time that spans nearly two decades of life. Processes that govern species-specific aspects of human postnatal brain development are difficult to study in animal models[1]. While human brain organoids offer a promising in vitro model, they have thus far been shown to largely mimic early stages of brain development. Here we develop human brain organoids for 5 years in culture, optimizing growth conditions to extend excitatory neuron viability beyond previous limits. Using maturation-associated modules derived from endogenous human brain, we show that brain organoids transcriptionally age with cell type specificity over years in culture. Whole-genome methylation profiling reveals that the predicted epigenomic age of organoids correlates precisely with time spent in vitro, and parallels epigenomic ageing in vivo. Notably, we show that in chimeric organoids generated by mixing neural progenitors of different ages, old progenitors rapidly produce late neuronal fates, skipping the production of earlier neuronal progeny, therefore showing that progenitors that age in organoids retain a memory of the time spent in vitro. The data indicate that human brain organoids can continue to mature and record the passage of time over many years in culture.

Human brain development is orchestrated by transcriptional programs defined by spatially and temporally regulated waves of gene expression. These gene expression patterns are tightly coordinated by dynamic changes in the activity of regulatory elements and epigenomic remodelling, ensuring the timely emergence of distinct neural cell types and the progressive maturation of the nervous system. In humans, brain development and maturation proceed at a much slower pace than in most other species, with cortical neurons requiring years to reach full maturity. This protracted timeline is preserved in all cell types generated in vitro from human pluripotent stem (hPS) cells, including cortical neurons, pointing at a cell-intrinsic clock that sets the pace of brain development, although its molecular mechanisms and functional significance remain to be elucidated[1,2]. Recent work has shown the importance of epigenetic barriers that enforce the slow timing of human neuronal maturation[1], and the role of species-specific rates of mitochondrial metabolism in influencing developmental tempo[3]. Human organoids could, in principle, be used to study these processes of human brain maturation, but existing models largely recapitulate earlier developmental processes, and most studies do not follow organoids over a sufficiently long time span. One report cultured organoids for up to 694 days, and used bulk RNA-sequencing (RNA-seq) and methylation arrays to profile whole organoids[4]. However, there is known variation in the ability of distinct cell types to survive over long periods in culture, especially neuronal populations. Moreover, beyond the continued presence of a cell type, there is a need to understand whether structural and functional properties such as neuronal architecture and coordinated circuit activity are present over years in culture. It is therefore important to resolve and analyse individual cell populations and their functional features across different modalities along these extended timelines. Without cell-type-specific knowledge, and in the absence of longer timelines of maturation, we currently lack understanding of the mechanisms by which the many individual cell types of the human brain mature in vitro, and whether they can measure and record time as they do in vivo.

Here we developed human cortical organoids for over 5 years in culture and integrated single-cell transcriptional information with

[1]Department of Stem Cell & Regenerative Biology, Harvard University, Cambridge, MA, USA. [2]Stanley Center for Psychiatric Research, Broad Institute of MIT and Harvard, Cambridge, MA, USA. [3]Department of Genome Regulation, Max Planck Institute for Molecular Genetics, Berlin, Germany. [4]Digital Health Cluster, Hasso Plattner Institute for Digital Engineering, Digital Engineering Faculty, University of Potdsdam, Potsdam, Germany. [5]McGovern Institute, Department of Brain and Cognitive Sciences, Massachusetts Institute of Technology, Cambridge, MA, USA. [6]Department of Molecular and Cellular Biology and The Center for Brain Science, Harvard University, Cambridge, MA, USA. [7]Klarman Cell Observatory, Broad Institute of MIT and Harvard, Cambridge, MA, USA. [8]Genentech, San Francisco, CA, USA. [9]Broad Institute of MIT and Harvard, Boston, MA, USA. [10]Present address: Department for Clinical Sciences and Community Health (DISCCO), University of Milan, Milan, Italy. [11]Present address: Department of Translational Neuroscience, University Medical Center Utrecht (UMCU), Brain Center, Utrecht University, Utrecht, The Netherlands. [12]These authors contributed equally: Irene Faravelli, Noelia Antón-Bolaños. ✉e-mail: paola_arlotta@harvard.edu

epigenetic, structural and functional data to build a comprehensive map of development and maturation across an unprecedented time span. The data indicate that human brain organoids record the passage of time following endogenous milestones and using similar epigenetic mechanisms. Importantly, progenitors in old organoids can recall the passage of time, like a memory of development that has already happened, to generate late progeny without repeating early developmental steps. The work demonstrates that a diversity of cells in organoids can develop over considerable time periods and are capable of both recording and recalling their developmental age. These systems provide a wealth of data on largely inscrutable periods of postnatal development of the human brain.

Cortical organoids age appropriately in culture

The development and maturation of human brain organoids follows the notoriously slow, neotenous pace of the endogenous human brain, which requires many years to reach adulthood[5–8]. To date, organoids have mostly been studied over timespans of a few months, and it remains unclear whether they can continue to mature and age in culture over many years to mimic aspects of postnatal maturation of the human brain that otherwise remain largely experimentally inaccessible. To investigate this possibility, we cultured human organoids of the cerebral cortex for over 5 years using a protocol that we published previously[7]. To characterize the cellular composition and molecular features of individual cell types in these long-term cultures, we used single-cell RNA-seq (scRNA-seq) analysis to profile 34 single organoids collected at 6 months, 9 months, and 1, 1.5, 2, 3, 4 and 5 years, and integrated these data with our previously published dataset of 76 single organoids profiled from 15 days to 6 months[6,7,9] (Fig. 1a,b, Methods and Supplementary Table 1; $n = 110$ organoids in total, from 34 new datasets and 76 previously generated datasets; $n = 424{,}720$ cells).

To correlate transcriptional changes in organoids over years in vitro with those occurring in the human brain over years in vivo, we used label transfer from reference datasets of endogenous human cortex[10,11] to estimate the transcriptional 'age' of organoid cells (Methods): early organoids (15 days to 2 months) mapped to first-trimester human fetal brains; 3 to 6 month organoids predominantly mapped to the second trimester; and the later stages (9 months to 5 years) progressively shifted towards mapping to late prenatal and postnatal ages (Fig. 1c). This suggested a temporal alignment with in vivo developmental trajectories, with postnatal-like signatures emerging in organoids after 12 months in culture.

To precisely assess transcriptional maturation, we used DIALOGUE[12] to identify gene modules correlated with age in endogenous human fetal and postnatal cortex datasets[10,11] (Fig. 1d–f, Extended Data Fig. 1a,b, Supplementary Information and Supplementary Table 2). Projecting these maturation modules onto the organoid time-series dataset revealed a strong correlation between in vivo age-related module scores and duration of in vitro development (Pearson's $r = -0.08$, 0.78, 0.35, 0.78 and −0.72 for multicellular programs (MCPs) 1–5, respectively), showing that cells in organoids preserve a sequential progression of gene expression programs associated with maturation in vivo.

DNA methylation, particularly at age-associated CpG sites, serves as a powerful molecular readout of biological age[13]. In vivo, in cortex and other tissues, the methylome is dynamic during early development, but eventually reaches high levels of DNA methylation that are stably maintained postnatally. Whole-genome bisulfite sequencing (WGBS) of single organoids at nine timepoints from 3 months to 5 years in culture showed that organoids follow a similar global pattern of progressive methylation and subsequent stability, with dynamics and features that resemble epigenetic features of endogenous tissues. Key cortical genes involved in fate acquisition and layer specification showed progressive, time-dependent gains in CpG methylation, particularly within CpG islands and DNA methylation valleys (DMVs; Fig. 1g,h, Extended Data Fig. 1c–g and Supplementary Tables 3 and 4; a detailed discussion is provided in the Supplementary Information).

When comparing with endogenous postnatal maturation programs, we found that cell-type-specific differentially methylated regions (cdDMRs) that are variable in neuronal and non-neuronal cells across human cortical development from 0 to 23 years[14] likewise vary in organoids, in a manner that is largely consistent with their in vivo dynamics (Extended Data Fig. 1h–k and Supplementary Information). Differential methylation analysis between the 3-month and 5-years timepoints identified 213 age-correlated DMRs, which were enriched in epigenetic features of known developmental importance, including CpG islands, DMVs and gene regulatory elements, and included many genes known to have key roles in the developing neocortex (Fig. 1i, Extended Data Fig. 2a–d, Supplementary Table 3 and Supplementary Information). Finally, organoids showed progressive CpA methylation (mCA; a non-CpG modification that is a hallmark of neuronal maturity[15]) (Extended Data Fig. 2e) at a set of 1,383 human fetal forebrain superenhancers that gain mCA during postnatal neuron development in vivo[15], indicating appropriate temporal regulation of mCA programs (Extended Data Fig. 2f,g).

Together, these results imply that the ongoing methylation dynamics observed in organoids over extended culture may reflect in vitro recapitulation of endogenous development and maturation epigenetic programs.

CpG sites that show reproducible gains or losses in methylation over time[16] have been used to create age clocks, correlating methylation with the temporal age of the tissue, in vivo[17]. To evaluate whether organoids capture features of biological ageing, we applied three epigenetic clocks: the Horvath pan-tissue clock[17], a human fetal brain-specific epigenetic clock[18] and a human cortex-specific DNA methylation clock (Fig. 1j–k). In both the Horvath and cortex-specific models, predicted DNA methylation age (DNAm age) tracked closely with culture time ($r = 0.88$–0.90; median absolute error: 7.25 and 20.04 months, respectively) (Fig. 1j,k). Similarly, estimates from the fetal brain clock showed positive relationship with culture duration ($r = 0.54$, $P = 0.056$; Extended Data Fig. 2h). To verify that the observed methylation changes were not primarily driven by proliferation, we confirmed that methylation at solo-WCGW tetranucleotide sites, which correlates with mitotic division history, remained stable (Extended Data Fig. 2i).

Collectively, these findings demonstrate that organoids are capable of preserving robust, time-resolved transcriptional and DNA methylation programs that are associated with tissue ageing in vivo. The ability to recapitulate transcriptional and epigenetic signatures of in vivo maturation across 5 years in vitro establishes organoids as a powerful model system to study the biology of both the prenatal and postnatal human brain.

APM medium maintains excitatory neurons

It is well known that not all cell types survive equally well in organoids, underscoring the importance of single-cell resolution when assaying long-term organoid cultures. Our scRNA-seq time course showed that all expected cell types were generated in cortical organoids (Fig. 2a,b, Extended Data Fig. 3a,b and Supplementary Table 5). Most broad cell types exhibited a significant correlation between age and MCP4 values, indicating that each population continued to mature over time in culture (Extended Data Fig. 3d,e). Reproducibility metrics, assessed using Aitchison distances, remained within the range of human tissue variability throughout the entire culture period (Extended Data Fig. 3c).

We next investigated whether individual cell types in organoids maintained molecular fidelity to the human reference over time. Across astrocytes and glial progenitors, which remained well-represented over the 5 years of culture, we found consistent mapping of time in vitro to

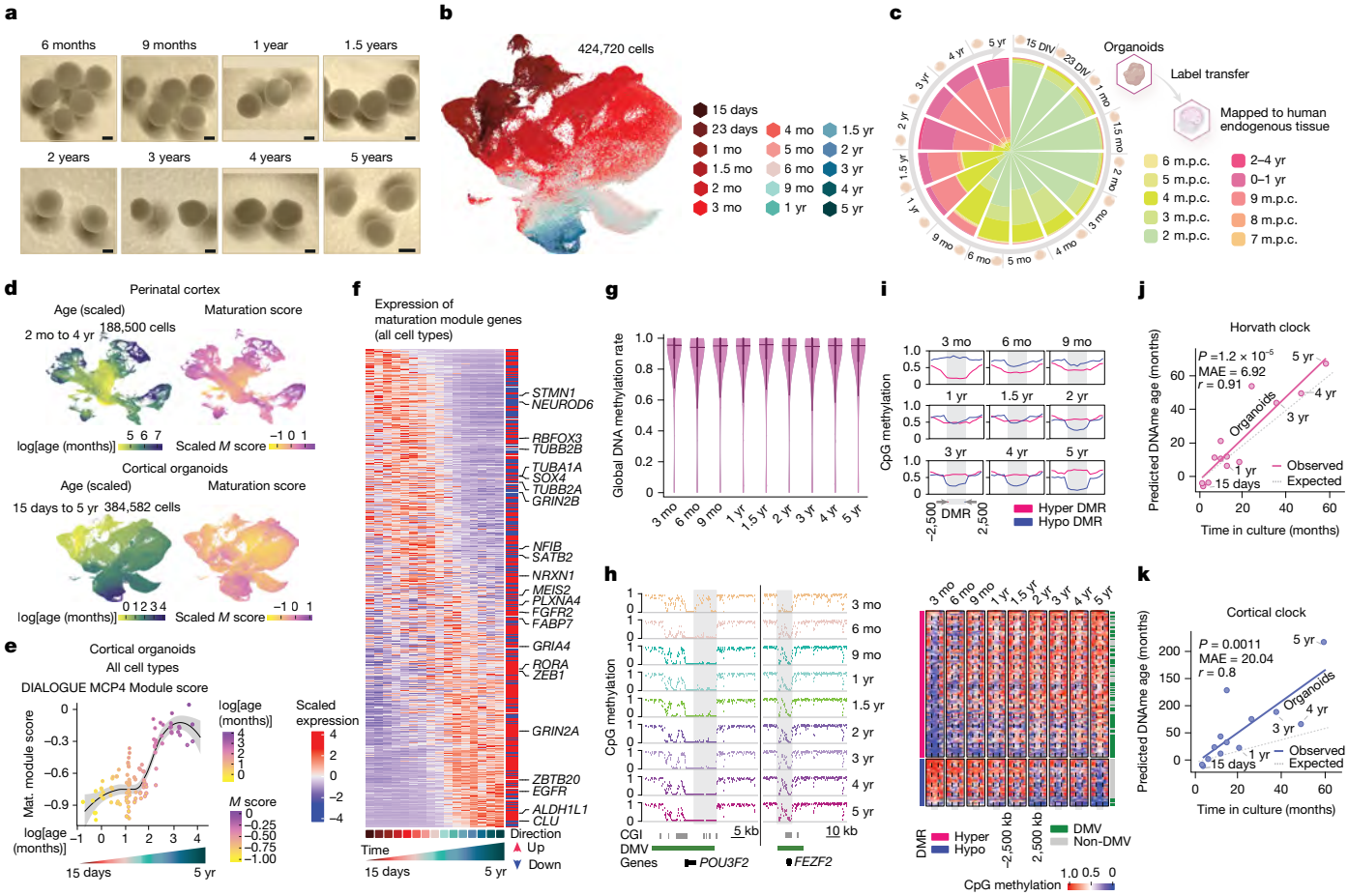


Fig. 1 | Cortical organoids undergo progressive maturation during long-term culture. a, Organoid time-series (*n* values are described in the Methods). Scale bars, 1 mm. **b**, Uniform manifold approximation and projection (UMAP) of scRNA-seq data coloured by cortical organoid ages. *n* = 424,720 cells across 16 timepoints. **c**, The age range of the endogenous perinatal human tissue[10,11] mapped to cells from each cortical organoid timepoint through label transfer. m.p.c., months post-conception. **d**, UMAPs of subsetted and renormalized data from endogenous perinatal tissue[10,11] and cortical organoids, coloured by the log-scaled age of each sample/organoid and the *z*-scored maturation score of each cell (Methods). **e**, The mean maturation score of all scored cells per organoid by log[age (months (mo))]. **f**, The expression of all MCP4 genes in organoids across time. The red/blue colour bar indicates genes in the up or down aspect of MCP4. Labelling highlights selected genes that exemplify biological features over time. **g**, Global CpG DNA methylation levels. The line in the violin plot indicates the median of the distribution. *n* = 23,720,371, 25,116,584, 24,229,564, 25,304,660, 25,373,110, 23,961,529, 25,176,645, 25,351,061 and 24,019,295 CpGs per sample across 9 organoid timepoints, respectively. **h**, Methylation profiles of DMRs (grey boxes) at the *POU3F2* and *FEZF2* loci across all timepoints. CpG islands (CGIs) and genes are annotated below. **i**, The average CpG methylation profiles across *n* = 164 hyper- and *n* = 49 hypo-DMRs identified between 3-month and 5-year organoids that show strong correlation with time in culture (Pearson correlation coefficient > 0.6) (top). Bottom, methylation profiles across these hyper- and hypo-DMRs. Overlaps with DMVs are indicated on the right. The depicted region includes the DMR (grey box) and ±2.5 kb. **j**,**k**, The predicted DNA methylation age for the set of Horvath (**j**) or cortical clock (**k**) CpGs (approximately 350), showing the chronological age of organoids (*x* axis) versus the predicted DNA methylation age of organoids (*y* axis) in months. The dashed line indicates perfect correlation; the solid line shows the linear regression of data (*r* value is shown). MAE, median absolute error.

progressively later human developmental ages (Extended Data Fig. 3f). Of the genes that showed statistically significant change over time in both endogenous and organoid glial populations (1,907 genes), the majority (80.2%) displayed concordant temporal trends between organoids and endogenous tissue, and no significantly enriched biological processes were detected in the minority (19.8%) that showed discordant correlation (Extended Data Fig. 3g). Importantly, gene set enrichment analysis (GSEA) revealed that the glial transcriptional changes in vivo and in vitro shared underlying molecular signatures (Extended Data Fig. 3h). Finally, DIALOGUE revealed the involvement of cell-type-specific genes with known developmental roles in age-correlated multicellular processes (Extended Data Fig. 4a). Consistent with this molecular evidence of glial maturation, organoids gained progressive evidence of myelination at both the ultrastructural and protein levels (Extended Data Fig. 4b,c), indicating the presence of myelinating oligodendrocytes by 6 months in culture.

We next considered neurons. In this culture condition (CDM4; Methods), we find that neuronal populations progressively declined in proportion over time in the scRNA-seq data, although we still detected a small cluster containing inhibitory and excitatory neuronal markers in the 5-year-old samples (Fig. 2a,b and Extended Data Fig. 3a,b). As the dissociation required for scRNA-seq may lead to differential death of fragile cells such as neurons, we assessed the presence of neurons using methods applicable to intact organoids. Cells expressing the neuronal marker NeuN were detected by immunohistochemistry at 2, 3, 4 and 5.8 years in culture, and the excitatory neuronal marker SATB2 at 5.8 years. In agreement, bulk RNA-seq analysis of whole organoids demonstrated expression of neuronal genes at 2 and 3 years (Extended Data Fig. 2j,k). Together, these results demonstrate that despite a progressive decline in neuronal representation over time, long-term organoids retain surviving neuronal populations even after nearly 6 years in culture. We conclude that while these culture conditions

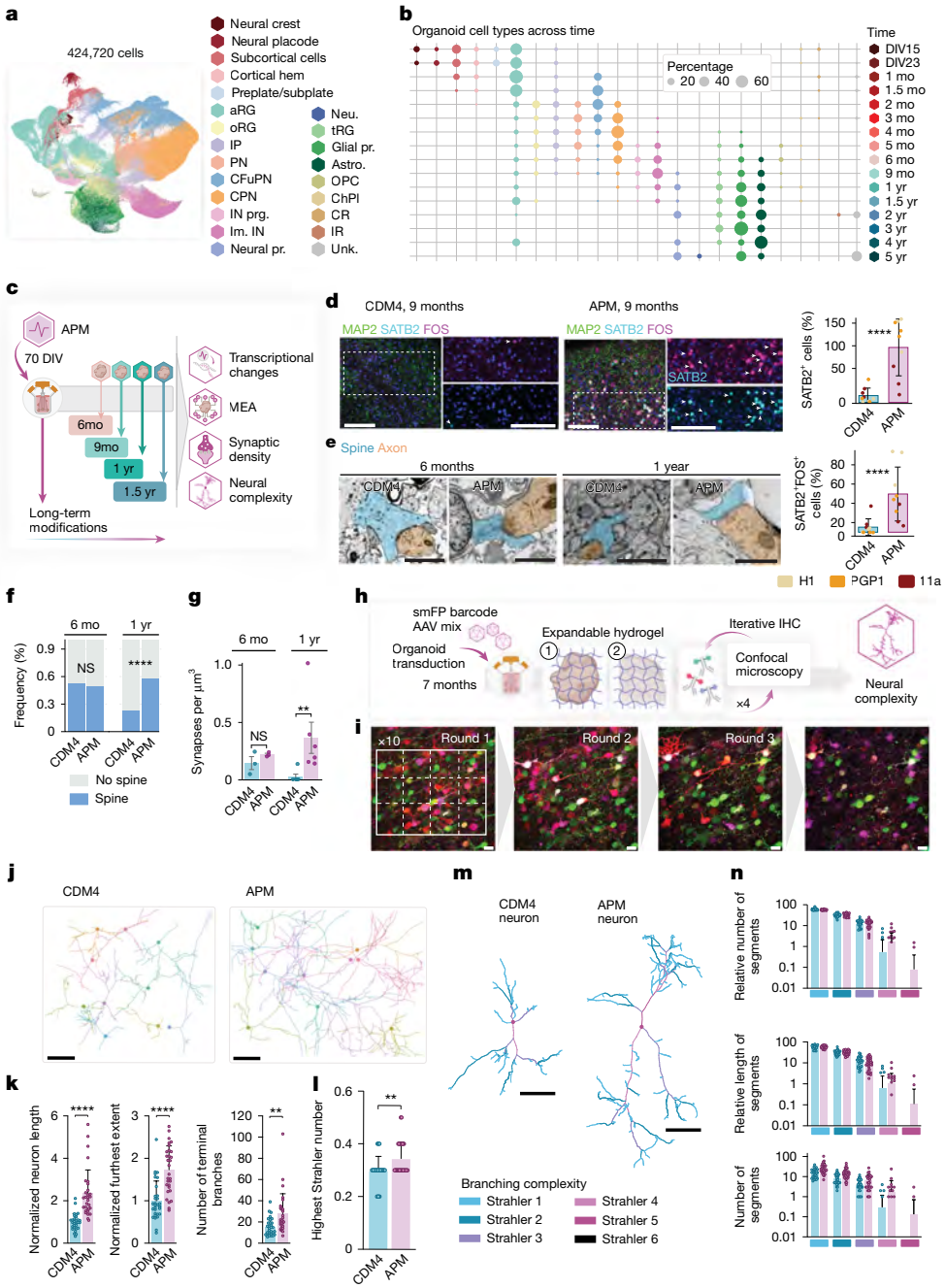


Fig. 2 | See next page for caption.

can maintain neurons over a span of years, they would benefit from further optimization to ensure consistent representation of neurons across extended timelines.

Spontaneous firing activity is known to have a role in neuronal survival, but conventional medium does not support robust activity. We therefore investigated a previously established medium designed to preserve spontaneous activity (BrainPhys)[19], to test whether it could improve neuronal survival in organoids. We used BrainPhys medium supplemented with GlutaMax to improve stability of glutamine and reduce ammonia accumulation[20] (hereafter, activity permissive medium (APM); Methods), and cultured organoids in APM starting from day in vitro 70 (DIV70; Fig. 2c). At 9 months, organoids cultured in APM showed a significant increase in the number of both callosal projection neurons (CPNs) ($SATB2^+$ cells) ($n = 9$ APM and 9 CDM4 organoids; linear mixed model (LMM), $P = 2.4 \times 10^{-5}$, 95% confidence interval (CI) = 68.1–144.4) and active CPNs ($SATB2^+FOS^+$ double-positive cells) ($n = 9$ APM and 9 CDM4 organoids; LMM, $P = 9.0 \times 10^{-4}$, 95% CI = 16.6–52.3) (Fig. 2d), consistent with an increased number of active neurons in the APM organoids.

To investigate whether APM promoted ultrastructural and morphological features associated with neuronal maturity and activity, we examined synapse density and synaptic spine formation using quantitative electron microscopy (EM) and neuronal morphology by expansion microscopy. EM with automated synapse detection[21] showed that, while no statistically significant differences in synaptic density were observed at 6 months (Wilcoxon rank-sum test, $P = 0.7$), at 1 year, APM organoids exhibited higher synaptic densities ($P = 0.002$) than CDM4 organoids (6 months: $n = 3$ organoids from each of $n = 2$ genetic backgrounds (H1 and 11a); 1 year: $n = 6$ organoids from each of $n = 3$ genetic backgrounds (H1, 11a and PGP1), for both CDM4 and

Fig. 2 | Activity-permissive medium maintains excitatory neurons. a, UMAP plot of scRNA-seq data coloured by cell type (110 organoids, 424,720 cells). Astro, astrocytes; ChPl, choroid plexus; CR, Cajal Retzius; im., immature; IN, interneuron; IR, interferon response; neu., neurons; pr., precursors; prg., progenitors; unk., unknown. **b**, The distribution of cell types by timepoint. The dot size represents the percentage abundance; the *y* axis represents the timepoint; and the *x* axis and colour represent the cell type. **c**, Schematics. **d**, Immunohistochemistry analysis of FOS (activity) and SATB2 (CPNs) in CDM4 (left) and APM (right) 9 month organoids. Scale bars, 100 µm. $SATB2^+$ and $SATB2^+FOS^+$ cells are significantly higher in APM versus CDM4 at 9 months in 3 different iPS cell lines ($n = 3$ per line; $P = 2.40 \times 10^{-5}$ and $P = 9.9 \times 10^{-5}$, respectively) (right). The bar plots show the mean total counts of $SATB2^+$ (top) and $SATB2^+FOS^+$ (bottom) cells. Data are mean ± s.d. LMEMs included cell line as a random effect. **e**, Representative EM images of synaptic compartments. CDM4: $n = 3$ (6 months) and $n = 6$ (1 year) organoids; APM: $n = 3$ (6 months) and $n = 6$ (1 year) organoids. Scale bars, 1 µm (left), 750 nm (middle left), 800 nm (middle right) and 680 nm (right). **f**, Quantification of the EM dendritic spine frequencies at 6 and 12 months. Two-sided Fisher's exact test on the raw count data; $P = 0.509$ (6 months) and $P = 9.47 \times 10^{-8}$ (12 months). **g**, Quantification of EM synaptic density at 6 and 12 months. The synaptic density between CDM4 ($n = 3$ (6 months) and $n = 6$ (1 year) organoids) and APM ($n = 3$ (6 months) and $n = 6$ (1 year) organoids) was compared using the two-sided Wilcoxon rank-sum test; $P = 0.70$ (6 months) and $P = 2.16 \times 10^{-3}$ (12 months). Data are mean ± s.e.m. **h**, Schematic of epitope tag barcoding and expansion microscopy workflow. **i**, Low-magnification overview of iterative immunohistochemistry (IHC). $n = 3$ organoids per treatment (APM and CDM4), $n = 10$ neurons per organoid. Scale bars, 100 µm. The white box indicates the area for high-magnification tile-scan imaging for neuronal tracing. **j**, Tracing and morphological reconstruction of ten representative individual neurons in the CDM4 and APM conditions. Scale bars, 162.5 µm. **k**, Quantification of neuron length normalized to CDM4 (two-tailed unpaired *t*-test, $P = 3.95 \times 10^{-8}$; left); the furthest extent normalized to CDM4 (unpaired *t*-test, $P = 8.75 \times 10^{-7}$; middle); and the number of terminal branches (two-tailed unpaired *t*-test, $P = 0.0018$; right). $n = 30$ traces per condition. **l**, Comparison of the highest Strahler number in the CDM4 and APM conditions. Two-tailed unpaired *t*-test, $P = 0.0034$. **m**, Visualization of Strahler analysis for one representative CDM4-cultured and APM-cultured PGP1 neuron at 7 months. Scale bars, 162.5 µm. **n**, Quantification of the absolute number, relative number and relative length of different Strahler number segments in the CDM4 and APM conditions. $n = 3$ organoids per treatment, $n = 10$ neurons per organoid, resulting in $n = 30$ traces per condition in **i**, **k**, **l** and **n**. For **k**, **l** and **n**, data are mean ± s.d. $^{**}P < 0.01$, $^{****}P < 0.0001$; NS, not significant.

APM conditions; Fig. 2e–g, Supplementary Table 6, Supplementary Videos 1 and 2 and Supplementary Information). Furthermore, at 1 year, a significantly higher proportion of synapses in the APM-treated organoids was located on spines (25% versus 52% in CDM4 and APM, respectively; two-sided Fisher's exact tests: 6 months: $P = 0.51$, odds ratio (OR) = 0.88, 95% CI = 0.60–1.30; 1 year: $P = 9.5 \times 10^{-8}$, OR = 4.67, 95% CI = 2.49–9.23; Fig. 2f and Supplementary Information). This is consistent with enhanced synaptic maturation and stabilization in APM organoids, features that are critical for the long-term integrity of synaptic circuits.

To assess neuronal complexity (that is, arborization and process outgrowth)—a clear measure of cortical neuron maturation in vivo—we used epitope tag barcoding[22–25] as a tracing strategy[26] in combination with antigenically orthogonal fluorescent proteins[27] and magnify expansion microscopy[28] (Fig. 2h,i, Extended Data Fig. 5a,b and Methods). At 7 months, APM-treated neurons exhibited significantly greater morphological complexity (total neurite length, maximal process extension and number of terminal branches), along with significantly higher maximum Strahler numbers—a measure of arborization complexity (Fig. 2j–n; a detailed discussion is provided in the Supplementary Information). Together, these results demonstrate that APM culture conditions promote both synapse development and increased neuronal morphological complexity.

To examine the effects of APM on cell proportions and transcriptional states over time, we performed scRNA-seq analysis of individual organoids from four different donors over a time course from 4 months to 1.5 years in culture (4 months: CDM4: $n = 6$, 15,972 cells; APM: $n = 2$, 4,579 cells; 6 months: CDM4: $n = 10$, 64,817 cells; APM: $n = 9$, 41,231 cells; 9 months: CDM4: $n = 6$, 18,104 cells; APM: $n = 3$, 8,533 cells; 1 year: CDM4: $n = 4$, 7,802 cells; APM: $n = 3$, 6,084 cells; 1.5 years: CDM4: $n = 2$, 3,952 cells; APM: $n = 2$, 8,670 cells; Fig. 3a–g and Extended Data Figs. 5c–e and 6 and Supplementary Table 7). Reproducibility, assessed using Atchison distances[9], demonstrated that, at all ages in both conditions, intersample variability fell within the limits of variation found in endogenous tissue (Fig. 3f and Extended Data Fig. 6j).

We examined the maintenance of excitatory neuronal populations, with particular focus on CPNs, a late-born population of excitatory neurons that are expanded in humans compared with other mammals and are associated with the evolution of higher cognitive functions[29]. Marked differences in cellular composition were apparent as early as 6 months (CDM4: $n = 10$ organoids, 64,817 cells; APM: $n = 9$ organoids, 41,231 cells): APM organoids showed increased proportions of excitatory neuron subtypes, including CPNs and corticofugal projection neurons (CFuPNs), while glial populations and inhibitory neurons were proportionately reduced (false-discovery rate (FDR)-adjusted $P = 1.15 \times 10^{-2}$ (apical radial glia, aRGs), 3.38×10^{-7} (outer radial glia, oRGs), 1.95×10^{-2} (intermediate progenitors, IPs), 9.23×10^{-8} (CFuPNs), 2.69×10^{-8} (CPNs), 1.24×10^{-5} (interneuron (IN) progenitors), 4.19×10^{-6} (immature INs), 4.81×10^{-2} (truncated radial glia, tRGs), 1.52×10^{-1} (glial precursors), 4.33×10^{-13} (astrocytes), 2.46×10^{-2} (oligodendrocyte progenitor cells, OPCs), negative binomial mixed-effect (NBME) model; Fig. 3b–g). Notably, the enrichment of CPNs was maintained at 9 months and 1 year (FDR-adjusted $P = 7.05 \times 10^{-3}$ (9 months) and 1.96×10^{-2} (1 year)) and, at 1.5 years, we observed an absolute increase in CPNs (3.04%) in APM compared with CDM4 (Fig. 3b and Extended Data Fig. 6). Together, this indicates that APM culture conditions selectively favour the long-term maintenance and stability of excitatory cortical neurons, including CPNs.

Consistent with our findings in EM and morphological analysis, neurons from APM organoids showed increased gene module scores for synapse-related genes (6 months: $n = 9$ APM and 10 CDM4 organoids; LMM, $P = 0.022$, expected increase = 1.03, 95% CI = 1.01–1.05; Methods, Extended Data Fig. 7 and Supplementary Tables 8 and 9). Likewise, Gene Ontology (GO) analysis showed enrichment of GO terms related to synapse organization and function in excitatory neurons from APM organoids (Extended Data Fig. 7e and Supplementary Table 10).

To understand whether APM may change neuronal proportions by differentially affecting the proliferation of neural progenitors, we quantified actively cycling cells using Seurat module scores (Methods). APM increased the proportion of cycling aRG cells (binomial linear mixed-effects model (LMEM): $n = 7{,}941$ APM cells, 8,808 CDM4 cells; $P = 1.2 \times 10^{-11}$, OR = 8.76, 95% CI = 5.25–14.62), whereas CDM4 preferentially enhanced proliferation in interneuron progenitors (binomial LMEM: $n = 2{,}390$ APM cells, 8,984 CDM4 cells; $P = 3.7 \times 10^{-5}$, OR = 0.07, 95% CI = 0.02–0.21), indicating that the two media favour the expansion of different cell populations, even though all cell types were still represented (Extended Data Fig. 6k and Supplementary Table 11).

Analysis of metabolic heath indicated that transcriptional stress signatures were primarily found in progenitor populations, and that the hypoxia signal was largely confined to the organoid core, consistent with previous observations[6] (Extended Data Fig. 8a–e, Supplementary Table 11 and Supplementary Information). Notably, excitatory neuronal populations under APM conditions showed no increase over time in any stress-related signatures, indicating sustained neuronal health in APM (LMEM; apoptosis: $P = 0.24$, hypoxia: $P = 0.79$; glycolysis: $P = 0.42$; Extended Data Fig. 8f).

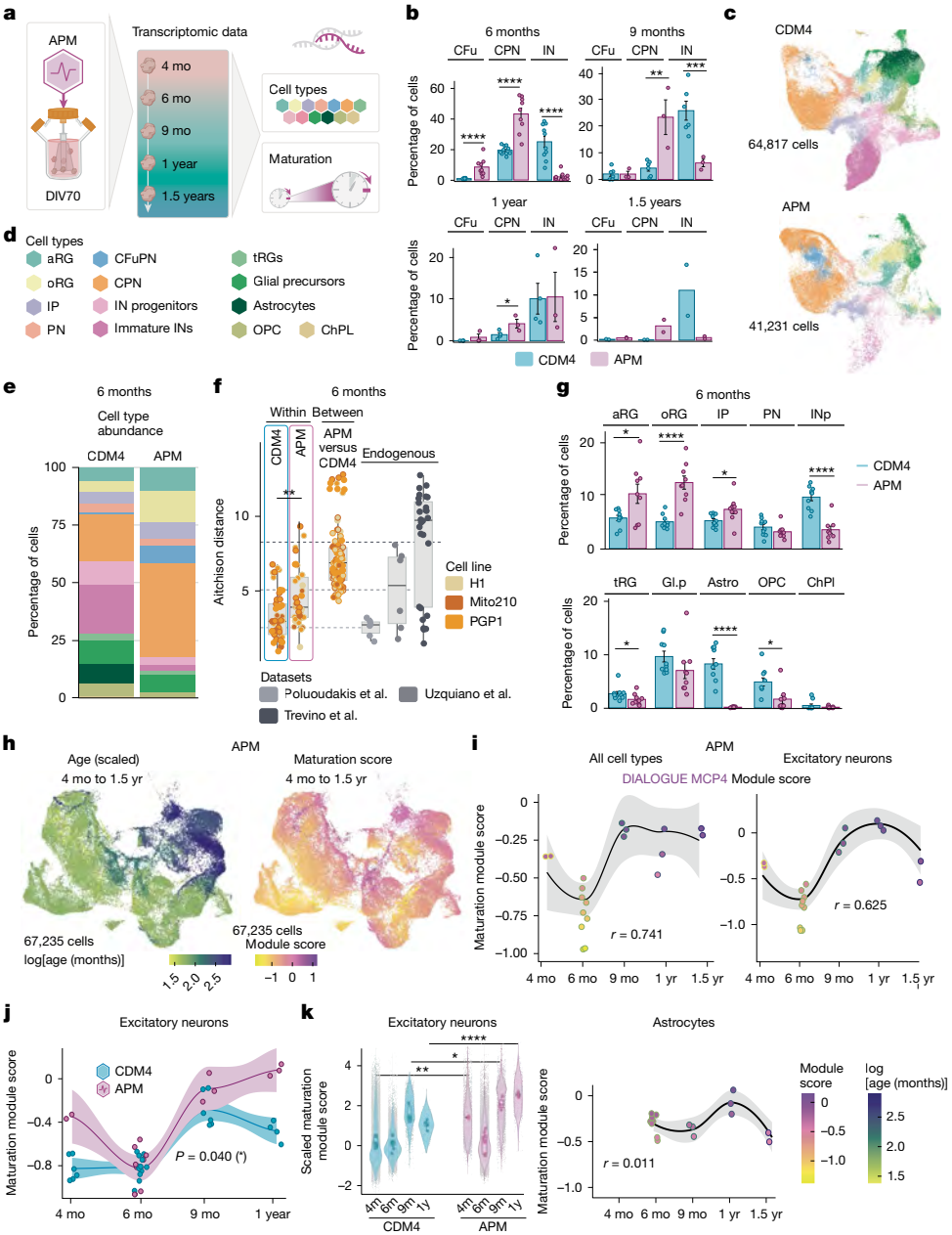


Fig. 3 | Activity-permissive medium enhances the maturation of cortical organoids. a, Schematic of the experiment. **b**, Changes in the neuronal proportions between CDM4- and APM-treated organoids at 6 months ($n = 10$ (CDM4) versus $n = 9$ (APM)), 9 months ($n = 6$ (CDM4) versus $n = 3$ (APM)), 1 year ($n = 4$ (CDM4) versus $n = 3$ (APM)) and 18 months ($n = 2$ per treatment). Data are the mean ± s.e.m. percentage of cell types. FDR-adjusted P values (one-sided likelihood ratio test) are denoted by asterisks; $^{*}P < 0.05$, $^{***}P < 0.001$ (Methods and Supplementary Table 7). **c**, UMAP of integrated scRNA-seq data from 6-month CDM4-treated ($n = 64{,}817$ cells, 10 organoids) and APM-treated ($n = 41{,}231$ cells, 9 organoids) organoids, coloured by cell type. **d**, Annotated cell types. **e**, Cell type proportions. **f**, The Aitchison distances between cell type compositions of unique pairs of replicates within and between treatments at 6 months. Within-treatment distances were compared using two-sided Wilcoxon rank-sum tests; $P = 1.21 \times 10^{-3}$. $n = 45$ (CDM4) versus $n = 36$ (APM). The box plots show the median (centre line) and interquartile range (IQR) and the whiskers show 1.5 × IQR. The dotted lines show the mean Aitchison distances in human endogenous datasets[6,38,39]. **g**, Changes of other cell type proportions between CDM4- and APM-treated organoids at 6 months. Analysis and representation was as described in **b**. Gl.p, glial progenitors. **h**, UMAP of scRNA-seq data of APM-treated organoids (4 to 18 months; $n = 67{,}235$ cells from 19 organoids), coloured by log[age (months)] (left) and the z-scored DIALOGUE MCP4 maturation score (right). **i**, Age-dependent trends in the DIALOGUE MCP4 maturation score along developmental timepoints in APM-treated organoids. Jittered dots show the averaged scores across all cells or by cell population (astrocytes and excitatory neurons (CFuPNs, CPNs and PNs)) for each organoid. The black lines show smoothed conditional means; the grey regions show the 95% CIs. **j**, In excitatory neurons, APM-treated organoids show increased DIALOGUE maturation scores in a time-series manner. $n = 29{,}452$ cells from 26 organoids (CDM4) and $n = 27{,}337$ cells from 17 organoids (APM). One-sided F-test, $P = 4.0 \times 10^{-2}$ (Methods). **k**, In excitatory neurons, APM-treated organoids show significantly higher DIALOGUE MCP4 maturation scores at 4, 9 and 12 months. Statistical P values were derived using the one-sided likelihood ratio test comparing LMEMs, comparing CDM4 versus APM; $P = 1.56 \times 10^{-3}$ (4 months), $P = 9.77 \times 10^{-1}$ (6 months), $P = 5.88 \times 10^{-2}$ (9 months), $P = 3.86 \times 10^{-6}$ (1 year). 4 months: $n = 11{,}671$ cells and 6 samples (CDM4) versus 2,717 cells and 2 samples (APM); 6 months: $n = 16{,}361$ cells and 10 samples (CDM4) versus 21,434 cells and 9 samples (APM); 9 months: $n = 1{,}303$ cells and 6 samples (CDM4) versus 2,859 cells and 3 samples (APM); 1 year: $n = 117$ cells and 4 samples (CDM4) versus 327 cells and 3 samples (APM). The grey dots and violin plots show cell-level scores and distributions. The coloured dots show the organoid means, the box centre line shows the median, the box limits show the IQR and the whiskers show 1.5 × IRQ.

To evaluate transcriptional maturation, we again applied the DIALOGUE-based module scoring approach described in Fig. 1d. As in the CDM4 organoids, APM organoids showed strong correlation between time in culture and maturation module score ($n = 19$ organoids; Pearson's $r = 0.741$) (Fig. 3h,i). Importantly, this approach enabled a direct comparison between excitatory neurons in APM- and CDM4-cultured organoids between 4 months and 1 year (the age at which neuronal representation declines in CDM4 datasets). Excitatory neurons in APM organoids scored consistently higher in maturation index (one-sided F test, $P = 4.03 \times 10^{-2}$, linear models) (Fig. 3j); these differences were significant at all timepoints except for 6 months (likelihood ratio test P values, 4 months, 1.56×10^{-3}; 6 months, 9.77×10^{-1}; 9 months, 5.88×10^{-2}; 12 months, 3.86×10^{-6}; LMEMs) (Fig. 3k).

Finally, we examined whether activity-permissive culture conditions resulted in corresponding changes in the DNA methylome. Comparative WGBS of organoids cultured in CDM4 or APM at matched timepoints (9 months and 1 year; Extended Data Fig. 9a) identified around 900 DMRs between culture conditions (Extended Data Fig. 9b). Notably, these condition-associated DMRs were enriched for neuron-associated and maturation-related genes (Extended Data Fig. 9c,d and Supplementary Table 12). Despite these locus-specific differences, the overall directionality and temporal structure of age-associated methylation remodelling were preserved across culture conditions. Both CDM4- and APM-cultured organoids showed strong correlation between methylation age and time (Extended Data Fig. 9e).

It is unclear whether organoids can build and maintain active neuronal circuits over years in culture. We therefore directly compared neuronal and network activity between culture conditions. We recorded spontaneous extracellular activity using a three-dimensional (3D) multielectrode array (MEA) platform[9] (Methods) from both APM and CDM4 organoids at 6, 9 and 12 months of differentiation (total of 19 single organoids from three different donor lines; Fig. 4), comparing organoids that were cultured continuously in APM starting from DIV70, to control organoids derived from the same lines that were cultured in conventional medium (CDM4) and transferred to APM 2 weeks before recording as previously described[30]. For each organoid, we recorded a minimum of 20 min of spontaneous activity and identified spikes post hoc using kilosort[31], which we optimized for application to organoids (Methods). The majority of recorded organoids under both APM and CDM4 conditions exhibited periodic bursts of highly correlated activity, known as network bursts. Pharmacological treatment verified that the signal corresponded to action potentials and bursting was mediated by synaptic glutamatergic transmission (Methods and Extended Data Fig. 10a,b). Across all three ages, APM organoids displayed a higher spike rate (analysis of variance (ANOVA), $P = 2.60 \times 10^{-4}$) and increased network burst frequency (ANOVA, $P = 4.87 \times 10^{-3}$) (Fig. 4b, Supplementary Table 13, Extended Data Fig. 10c,d and Supplementary Video 3), more spikes per burst (ANOVA, $P = 1.25 \times 10^{-8}$) and a greater number of neurons participating in each burst (ANOVA, $P = 1.76 \times 10^{-7}$) (Fig. 4b and Extended Data Fig. 10c,d). Notably, starting from 9 months of differentiation, APM organoids displayed more complex bursting patterns, while CDM4 organoids showed increasingly sparse activity over the same period (Fig. 4c and Extended Data Fig. 10c,d). The most pronounced differences between the two conditions were observed at the 1-year mark: organoids cultured in CDM4 for 1 year consistently failed to exhibit any network bursts (8 out of 8), whereas all APM organoids at 1 year exhibited robust network bursts (9 out of 9).

Notably, recordings from APM organoids that had been maintained in culture for 2 years still showed active bursting, indicating that APM supports the continued presence of active, functional neurons over multiyear timelines (Fig. 4d, Extended Data Fig. 10e and Supplementary Video 4). Notably, the structure of these bursts differed from younger organoids. In organoids that are one year old or younger, when network/population bursts were observed (either in CDM4 or APM), the majority of neurons participate in these events. These neurons fire during every burst, indicating a single, homogeneous mode of collective activation. By contrast, in two-year-old APM-cultured organoids, at least two distinct neuronal subgroups could be identified during bursts, each displaying its own form of collective activation, characterized by unique frequencies, amplitudes and participating neuronal populations (Fig. 4d). In agreement with the functional data, 2-year-old APM-cultured organoids showed the presence of $NeuN^+$ neuronal cells by immunohistochemistry (Fig. 4e).

Taken together, these results show that promoting neuronal activity through culture in activity-permissive medium results in the maintenance of functional neuronal populations for at least 2 years in culture. Neurons produced in organoids under these conditions display greater morphological and transcriptional maturity compared with conventional medium, while still being generated according to endogenous molecular programs of development. Notably, our ability to maintain and profile excitatory neurons over these extended culture periods has enabled the generation of a comprehensive multi-modal dataset, comprising molecular, morphological and electrophysiological data on human excitatory cortical neurons at an unprecedented, advanced stage of in vitro development.

Progenitors record and recall developmental time

Elegant work in the developing mouse and chick embryos has shown that developing cells track developmental time, progressively restricting their fate potential to execute temporally appropriate developmental programs even if transplanted into a heterochronic host[32,33]. As a measure of functional changes over time in organoids, we tested whether cells in older organoids retain a memory of the time spent in culture; specifically, whether cells of different ages would show distinctions in fate potential, manifested as their ability to generate early versus late progeny.

To this end, we first tested whether co-development of progenitors of different ages inside the same organoid could be used to probe the differential fate potential of neural progenitors developed for longer or shorter periods of time. For this, we developed an ex vivo mouse chimeroid system using progenitors derived from the embryonic mouse brain (Supplementary Information), as it gives the distinct advantages of fast development and endogenous origin of the progenitor cells. Young organoids (generated from dissociated embryonic day 11.5 (E11.5) mouse cerebral cortex) were cultured for 2 to 3 weeks to generate 'old' organoids (Extended Data Fig. 11a–d). We confirmed that neuronal cells were not carried over through dissociation and reaggregation of chimeroids using AAV PHP.eB labelling[34–36] (Extended Data Fig. 11e,f), consistent with our previous findings in human cortical chimeroids[9].

To create chimeroids, we either mixed progenitors from the 2-to-3-week-old organoids alone (monochronic), or mixed cells from the 2-to-3-week-old organoids with freshly dissociated, young, E11.5 cells (heterochronic; Extended Data Fig. 11g). At 1 day after aggregation, old monochronic mouse cultures showed minimal $SATB2^+$ cells, while the heterochronic condition exhibited significantly more (ANOVA, $P = 6.14 \times 10^{-17}$, Tukey post hoc $P = 2.35 \times 10^{-14}$) (Extended Data Fig. 11h). Control 'young' monochronic chimeroids (derived from E11.5 cortex without previous culture) took longer to begin to produce $SATB2^+$ cells, consistent with the fact that they had not yet completed earlier developmental steps (Extended Data Fig. 11i and Supplementary Table 14). Together, these findings indicate that this system can be used to test the fate potential of progenitors.

To test whether human progenitors similarly change their fate potential as a reflection of the time passed in culture, we produced human chimeroids[9] by mixing either old cells (from organoids collected at

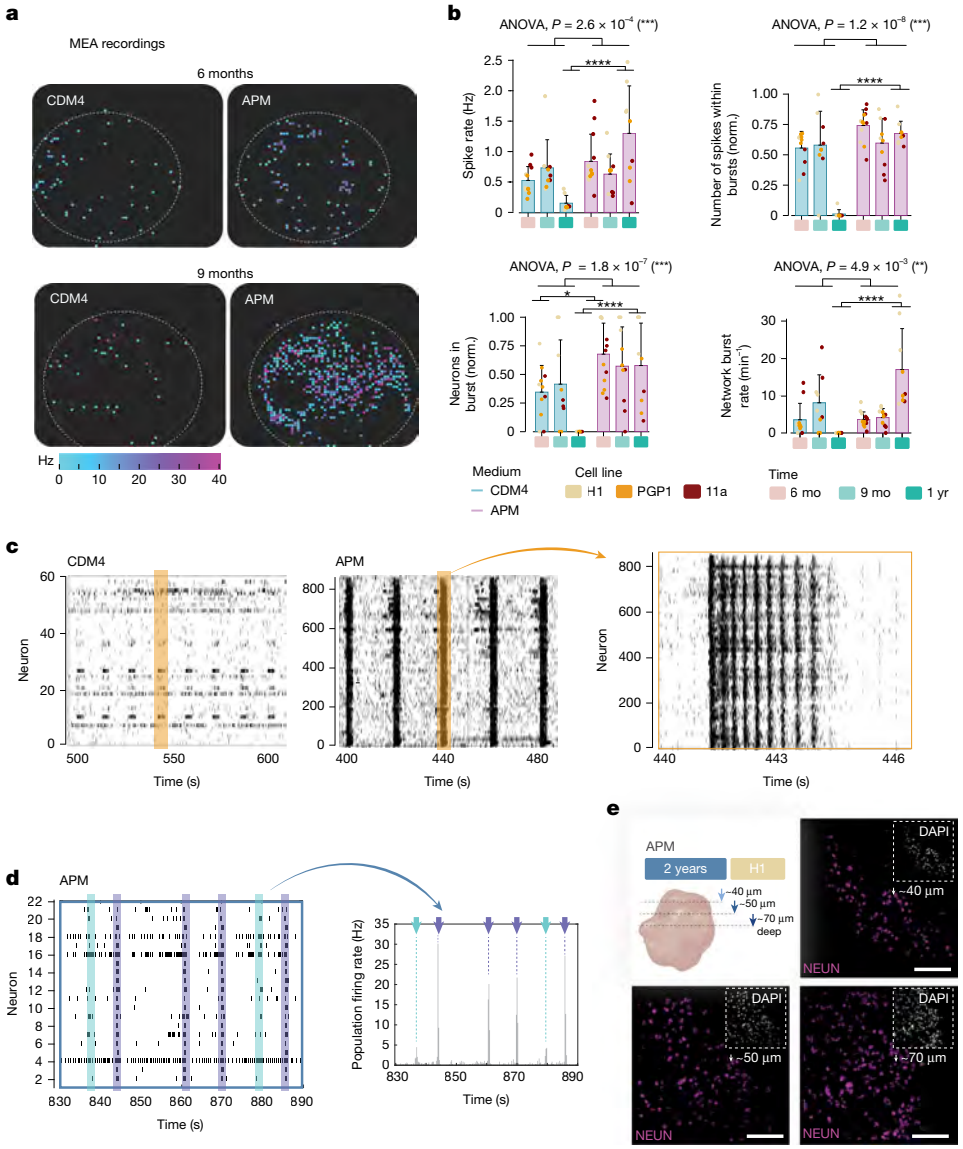


Fig. 4 | Activity-permissive medium maintains functional neuronal networks for at least 2 years in culture. a, Representative images of MEA recordings. **b**, For each metric measured by MEA, type III two-way ANOVA was performed to assess the effects of treatment, age and their interaction (treatment:age). For CDM4 versus APM, $n = 11$ versus 13 samples (6 months), $n = 9$ versus 10 samples (9 months) and $n = 8$ versus 9 samples (1 year). For cases in which quantifications of more than one cell line were available, the genetic background was included as a fixed effect. ANOVA P values are shown to denote the significance of the treatment effect on the measured metric, as represented by asterisks. Post hoc Tukey tests were performed to determine at which age the treatment significantly differ and P values adjusted using the Tukey's honest significant difference method are indicated by asterisks. Data are the mean ± s.d. of measured values. **c**,**d**, Representative raster plots of 9-month CDM4- and APM-cultured PGP1 organoids (**c**) and a 2-year APM-cultured H1 organoid (of $n = 4$ analysed) (**d**). **e**, Immunohistochemistry analysis of an APM-cultured H1 organoid at 2 years, showing NeuN-positive staining (mature neuronal marker) at different depths. Scale bars, 100 µm.

9–12 months), or a combination of old and young (from organoids at DIV15) cells.

First, we produced old monochronic chimeroids (monochronic (old)) from late-stage cortical organoids (9–12 months old) (Fig. 5a,b), and profiled pooled chimeroids (15–20 chimeroids per batch) at DIV15–19 after reaggregation using scRNA-seq. The monochronic (old) samples mirrored the cellular composition expected for organoids grown for 9 months of culture, containing all major cell types (over 5% abundance) found in standard organoids at 9 months. Of these major cell types, the monochronic (old) samples had a reduced prevalence of glial precursors (negative binomial generalized LMEM, $P = 8.5 \times 10^{-4}$) and oRGs ($P = 0.038$); the abundances of immature INs, IN progenitors, tRGs, aRGs and astrocytes were not significantly different ($P > 0.1$), despite the monochronic (old) chimeroids having developed for only 15 days after reaggregation (Fig. 5a,c,d and Supplementary Tables 5 and 14). Both were distinct from the cell types made in young chimeroids at DIV15 (aRGs, IPs, subplate cells, cortical hem cells, subcortical populations, Cajal Retzius cells and choroid plexus cells)[9]. This suggests that old progenitors retain a memory of the time they had previously spent in culture, producing progeny that is appropriate for their age (9–12 months), such as astroglia.

It is possible that the continued production of late cell types in the monochronic (old) chimeroids may be the result of a lack of signals instructive of earlier fates within these chimeroids. We therefore tested the fate potential of these old progenitors when exposed to instructive conditions from early cell fates by co-culture with cells from younger organoids (heterochronic chimeroids, or heterochronic). Progenitors from late-stage cortical organoids (9 to 12 months old) were mixed

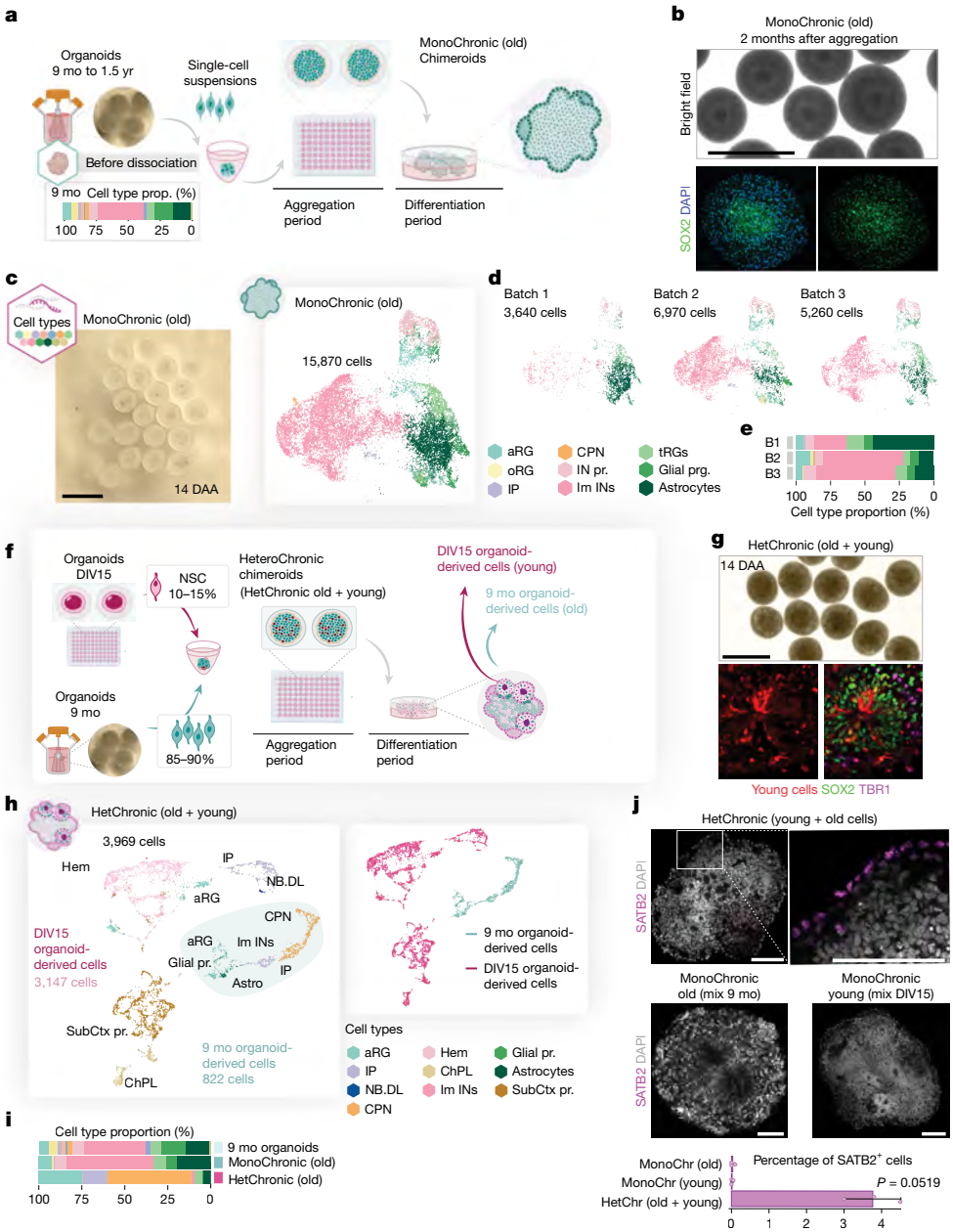


Fig. 5 | Organoid progenitors record and recall developmental time. **a**, Monochronic culture generation, including a stacked bar plot (bottom) showing the cell type composition of 9-month organoids. Prop., proportion. **b**, Representative bright-field image of monochronic (old) chimeroids ($n = 25$ per batch, 3 batches) and immunostaining ($n = 3$). Scale bar, 1 mm. **c**, Representative bright-field image ($n = 25$ per batch, 3 batches) and UMAP plot showing cells from monochronic (old) chimeroids ($n = 15{,}870$ cells from 3 chimeroids), coloured by cell type. Scale bar, 1 mm. DAA, days after aggregation. **d**, UMAP of monochronic (old) chimeroids split by sample. **e**, Cell type proportions. **f**, Schematic of heterochronic (old + young) generation. NSC, neural stem cells. **g**, Representative bright-field image of heterochronic chimeroids (old + young) ($n = 25$ per batch, 3 batches) and immunostaining ($n = 3$). Scale bar, 1 mm. **h**, UMAP plot showing cells from a heterochronic sample ($n = 3{,}969$ cells), coloured by cell type of the old and young counterparts (left). Right, UMAP plot showing cells from a heterochronic sample, coloured by temporal groups of cells (old and young). **i**, The relative proportion of cell types within 9-month organoids, the 9-month monochronic (old) chimeroids and the 9-month-old portion of the heterochronic (old + young) chimeroids. **j**, SATB2 immunostaining and quantification (bottom) across monochronic (old, $n = 3$), monochronic (young, $n = 3$) and heterochronic (old + young, $n = 3$) organoids. Scale bar, 100 µm. Kruskal–Wallis rank-sum tests were used to compare the differences between the groups; $P = 0.0519$. Data are the mean ± s.d. percentage of SATB2$^+$ cells (bottom).

with developmentally asynchronous progenitors from young organoids (DIV15), and profiled using scRNA-seq at DIV15 after aggregation (Fig. 5f–h). To resolve the originating organoid (and therefore age) contributing to each differentiated cell type in the chimeroids, we used different donor cell lines for young (PGP1) and old (GM) organoids[9,37] (Methods). Notably, old progenitors within heterochronic cultures (that is, those derived from the 9 month organoids) exhibited lower maturation scores than progenitors from monochronic (old) cultures (Extended Data Fig. 11j). Similarly, GSEA of genes that change during ageing from 6 to 9 months in canonical cortical organoids showed that old progenitors in heterochronic organoids shared a greater proportion of molecular programs with 6-month progenitors than monochronic (old) progenitors did (Extended Data Fig. 11k). Together, these results indicate that the younger cells in the heterochronic cultures provided instructive signals that the older cells are able to respond to.

Notably, derivatives of the old cells in heterochronic organoids showed a substantially higher proportion of CPNs (49.0%) compared with both the monochronic (old) group (replicate 1 = 0.55%, replicate 2 = 0.50%, replicate 3 (11 months) = 0.02%) and 9-month standard organoids (CPNs; 1.1%) (Fig. 5h,i). In agreement, while both old (9 month) and young (1 month) monochronic cultures had few or no putative CPNs ($SATB2^+$ cells), $SATB2^+$ putative CPNs were clearly detected in the heterochronic condition by immunohistochemistry (all assayed at DIV15 after reaggregation; Fig. 5j). These results indicate that exposure to inductive signals from young progenitors induced the old progenitors to restart excitatory neurogenesis, which occurs before astrogliogenesis. Notably, while the young-derived cells within the same heterochronic chimeroids produced only the early cell types expected at DIV30 (15 DIV + 15 DIV after aggregation), including cortical hem cells, subcortical precursors, aRGs, IPs, newborn deep-layer neurons and choroid plexus, the old progenitors produced CPNs, glial precursors and astrocytes, late-derived populations that are normally produced at 2–3 months of culture. Thus, in only 2 weeks after reaggregation, the old progenitors can generate late-stage neurons (CPNs), while their young progenitor counterparts produce much earlier cell fates within the same chimeric organoid.

Together, the human and mouse results indicate that cortical organoid cells retain a form of temporal memory. In human organoids, old progenitors are still plastic after 9 months in culture and can respond to instructive neurogenic signals to make excitatory neurons again; however, they have recorded the passage of time and retain a memory of the developmental steps already performed, such that even when exposed to signals instructive of an earlier neurogenic fate, they 'skip' production of early progeny to generate excitatory neurons normally produced after months in culture.

Discussion

The speed of development of cells and organs is markedly different across species[3]. The human brain displays extremely long periods of neoteny, taking close to two decades to form and mature. Human brain organoids that can continue to develop over years, rather than weeks and months, offer a unique opportunity to experimentally access species-specific processes of human brain postnatal maturation that cannot be easily accessed in vivo.

By enabling culture of human brain organoids for over 5 years, we demonstrate that organoids develop through similar transcriptional and epigenetic programs associated with age progression in the human brain in vivo, eventually acquiring features of human postnatal ages. These findings demonstrate that temporally structured regulation of cortical development can unfold over unprecedented timescales, even outside the context of the body.

It is notable that, during this process, organoids record the passage of time, and can also recall the time spent in culture, as shown by the fact that cells derived from old organoids can skip steps of development that they have already performed, and generate in 2 weeks late neuronal progeny that would normally take over 2 months to produce.

The data provide additional motivation for efforts to further integrate into organoid systems additional driving forces that shape brain development in vivo. Our demonstration that promoting spontaneous activity in organoids can support neuronal health and maturation over multiple years points at the potential benefit of incorporating factors that have been demonstrated to be critical for brain development in vivo, such as evoked activity through sensory systems and the influence of non-neural tissues.

Together, organoids cultured over extended timelines and the multimodal wealth of data produced from them represent both a powerful experimental system and the information to fuel understanding of the largely unexplored mechanisms governing human brain neoteny, maturation and evolution.

Online content

Any methods, additional references, Nature Portfolio reporting summaries, source data, extended data, supplementary information, acknowledgements, peer review information; details of author contributions and competing interests; and statements of data and code availability are available at https://doi.org/10.1038/s41586-026-10877-x.

1. Ciceri, G. et al. An epigenetic barrier sets the timing of human neuronal maturation. *Nature* **626**, 881–890 (2024).
2. Del Dosso, A., Urenda, J.-P., Nguyen, T. & Quadrato, G. Upgrading the physiological relevance of human brain organoids. *Neuron* **107**, 1014–1028 (2020).
3. Casimir, P., Iwata, R. & Vanderhaeghen, P. Linking mitochondria metabolism, developmental timing, and human brain evolution. *Curr. Opin. Genet. Dev.* **86**, 102182 (2024).
4. Gordon, A. et al. Long term maturation of human cortical organoids matches key early postnatal transitions. *Nat. Neurosci.* **24**, 331–342 (2021).
5. Fenlon, L. R. Timing as a mechanism of development and evolution in the cerebral cortex. *Brain Behav. Evol.* **97**, 8–32 (2021).
6. Uzquiano, A. et al. Proper acquisition of cell class identity in organoids allows definition of fate specification programs of the human cerebral cortex. *Cell* **185**, 3770–3788 (2022).
7. Velasco, S. et al. Individual brain organoids reproducibly form cell diversity of the human cerebral cortex. *Nature* **570**, 523–527 (2019).
8. He, Z. et al. An integrated transcriptomic cell atlas of human neural organoids. *Nature* **635**, 690–698 (2024).
9. Antón-Bolaños, N. et al. Brain Chimeroids reveal individual susceptibility to neurotoxic triggers. *Nature* **631**, 142–149 (2024).
10. Velmeshev, D. et al. Single-cell analysis of prenatal and postnatal human cortical development. *Science* **382**, eadf0834 (2023).
11. Wang, L. et al. Molecular and cellular dynamics of the developing human neocortex. *Nature* **647**, 169–178 (2025).
12. Jerby-Arnon, L. & Regev, A. DIALOGUE maps multicellular programs in tissue from single-cell or spatial transcriptomics data. *Nat. Biotechnol.* **40**, 1467–1477 (2022).
13. Moqri, M., Poganik, J. R., Horvath, S. & Gladyshev, V. N. What makes biological age epigenetic clocks tick. *Nat. Aging* **5**, 335–336 (2025).
14. Price, A. J. et al. Divergent neuronal DNA methylation patterns across human cortical development reveal critical periods and a unique role of CpH methylation. *Genome Biol.* **20**, 196 (2019).
15. Luo, C. et al. Cerebral organoids recapitulate epigenomic signatures of the human fetal brain. *Cell Rep.* **17**, 3369–3384 (2016).
16. Christensen, B. C. et al. Aging and environmental exposures alter tissue-specific DNA methylation dependent upon CpG island context. *PLoS Genet.* **5**, e1000602 (2009).
17. Horvath, S. DNA methylation age of human tissues and cell types. *Genome Biol.* **14**, R115 (2013).
18. Steg, L. C. et al. Novel epigenetic clock for fetal brain development predicts prenatal age for cellular stem cell models and derived neurons. *Mol. Brain* **14**, 98 (2021).
19. Bardy, C. et al. Neuronal medium that supports basic synaptic functions and activity of human neurons in vitro. *Proc. Natl Acad. Sci. USA* **112**, E2725–2734 (2015).
20. Perriot, S., Canales, M., Mathias, A. & Du Pasquier, R. Differentiation of functional astrocytes from human-induced pluripotent stem cells in chemically defined media. *STAR Protoc.* **2**, 100902 (2021).
21. Pavarino, E. C. et al. mEMbrain: an interactive deep learning MATLAB tool for connectomic segmentation on commodity desktops. *Front. Neural Circuits* **17**, 952921 (2023).
22. Dhainaut, M. et al. Spatial CRISPR genomics identifies regulators of the tumor microenvironment. *Cell* **185**, 1223–1239 (2022).
23. Kudo, T., Lane, K. & Covert, M. W. A multiplexed epitope barcoding strategy that enables dynamic cellular phenotypic screens. *Cell Syst.* **13**, 376–387 (2022).
24. Rovira-Clavé, X. et al. Spatial epitope barcoding reveals clonal tumor patch behaviors. *Cancer Cell* **40**, 1423–1439 (2022).
25. Wroblewska, A. et al. Protein barcodes enable high-dimensional single-cell CRISPR screens. *Cell* **175**, 1141–1155 (2018).
26. Park, S. Y. et al. Combinatorial protein barcodes enable self-correcting neuron tracing with nanoscale molecular context. Preprint at *bioRxiv* https://doi.org/10.1101/2025.09.26.678648 (2025).
27. Viswanathan, S. et al. High-performance probes for light and electron microscopy. *Nat. Methods* **12**, 568–576 (2015).
28. Klimas, A. et al. Magnify is a universal molecular anchoring strategy for expansion microscopy. *Nat. Biotechnol.* **41**, 858–869 (2023).
29. Berg, J. et al. Human neocortical expansion involves glutamatergic neuron diversification. *Nature* **598**, 151–158 (2021).
30. Paulsen, B. et al. Autism genes converge on asynchronous development of shared neuron classes. *Nature* **602**, 268–273 (2022).
31. Pachitariu, M., Sridhar, S., Pennington, J. & Stringer, C. Spike sorting with Kilosort4. *Nat. Methods* **21**, 914–921 (2024).
32. Oberst, P., Agirman, G. & Jabaudon, D. Principles of progenitor temporal patterning in the developing invertebrate and vertebrate nervous system. *Curr. Opin. Neurobiol.* **56**, 185–193 (2019).
33. Shen, Q. et al. The timing of cortical neurogenesis is encoded within lineages of individual progenitor cells. *Nat. Neurosci.* **9**, 743–751 (2006).
34. Mathiesen, S. N., Lock, J. L., Schoderboeck, L., Abraham, W. C. & Hughes, S. M. CNS transduction benefits of AAV-PHP.eB over AAV9 are dependent on administration route and mouse strain. *Mol. Ther. Methods Clin. Dev.* **19**, 447–458 (2020).

35. Fortuna, M. G. et al. AAV-PHP.eB achieves superior neuronal transduction over AAV9 in pigtail macaques following intracerebroventricular administration. *Mol. Ther. Methods Clin. Dev.* **33**, 101636 (2025).
36. Chan, K. Y. et al. Engineered AAVs for efficient noninvasive gene delivery to the central and peripheral nervous systems. *Nat. Neurosci.* **20**, 1172–1179 (2017).
37. Mitchell, J. M. et al. Mapping genetic effects on cellular phenotypes with "cell villages". Preprint at *bioRxiv* https://doi.org/10.1101/2020.06.29.174383 (2020).
38. Trevino, A. E. et al. Chromatin and gene-regulatory dynamics of the developing human cerebral cortex at single-cell resolution. *Cell* **184**, 5053–5069 (2021).
39. Polioudakis, D. et al. A single-cell transcriptomic atlas of human neocortical development during mid-gestation. *Neuron* **103**, 785–801 (2019).

Publisher's note Springer Nature remains neutral with regard to jurisdictional claims in published maps and institutional affiliations.

Open Access This article is licensed under a Creative Commons Attribution-NonCommercial-NoDerivatives 4.0 International License, which permits any non-commercial use, sharing, distribution and reproduction in any medium or format, as long as you give appropriate credit to the original author(s) and the source, provide a link to the Creative Commons licence, and indicate if you modified the licensed material. You do not have permission under this licence to share adapted material derived from this article or parts of it. The images or other third party material in this article are included in the article's Creative Commons licence, unless indicated otherwise in a credit line to the material. If material is not included in the article's Creative Commons licence and your intended use is not permitted by statutory regulation or exceeds the permitted use, you will need to obtain permission directly from the copyright holder. To view a copy of this licence, visit http://creativecommons.org/licenses/by-nc-nd/4.0/.

© The Author(s) 2026, modified publication 2026

Methods

Ethics statement

All experiments involving human cell lines were approved by the Harvard University IRB and ESCRO committees. All animal experiments were conducted according to protocols approved by the Institutional Animal Care and Use Committee (IACUC) of Harvard University. All experiments were performed in accordance with relevant guidelines and regulations, and in accordance with informed consent obtained from the donors of the originating cells or tissues.

Mouse experiments and housing

To develop the mouse-endogenous chimeroid system, we used wild-type CD-1 and C57BL/6 mice (Charles River Laboratories). We used embryos of both sexes, collected at E11.5. The sex of each embryo was not determined prior to the experiment. Sample size was not predetermined using specific methods. Mice were maintained under standard housing conditions in a temperature- and humidity-controlled facility under a 12 h–12 h light–dark cycle (light, 07:00 to 19:00) with ad libitum access to food and water. The ambient temperature was maintained at 20–24 °C and the relative humidity at 30–70%.

Human pluripotent stem cell culture

All human PS cell lines were maintained as previously detailed[7,9]. In brief, MTESR1 medium (StemCell Technologies), mTESR$^+$ medium (StemCell Technologies) or StemFlex medium (Gibco), all with 1% of added penicillin–streptomycin Solution (Corning), were employed for culture of stem cells in cell culture dishes (Falcon) precoated with 1% Geltrex (Gibco), at 37 °C in 5% CO_2. All human PS cells were maintained below passage 55 and tested negative for mycoplasma (assayed using the MycoAlert PLUS Mycoplasma Detection Kit, Lonza).

Characterization of the PS cell lines

The psychiatric control Mito210 male iPS cell line was provided by B. Cohen (McLean Hospital); the PGP1 male iPS cell line was provided by G. Church; the GM08330 male iPS cell line was provided by M. Talkowski (MGH) and was originally derived from fibroblasts obtained from the Coriell Institute for Medical Research[6,7,30]. The H1 male human embryonic stem cell line (also known as WA01) was purchased from WiCell; and the 11a iPS cell line was obtained from the Harvard Stem Cell Institute. The female CW50037 iPS cell line was from the California Institute for Regenerative Medicine (CIRM) iPS cell collection. All lines were authenticated as follows. The PGP1 iPS cell line was authenticated by short-tandem-repeat (STR) analysis (performed by TRIPath). The 11a cell line was authenticated by karyotyping as previously described[40]. The Mito210 iPS cell line was authenticated with genotyping analysis (Fluidigm FPV5 chip) performed by the Broad Institute Genomics Platform. The CW50037 iPS cell line was authenticated using single-nucleotide polymorphism (SNP) genotyping (Illumina Global Screening Array (GSA) from Illumina; processed at the Genomics Platform, Broad Institute) for cell line identification and detection of chromosomal abnormalities. The H1 and GM08330 lines were authenticated by STR analysis (performed by WiCell). The GM08330 parental line has a previously reported[30] interstitial duplication in the long (q) arm of chromosome 20; all other lines were karyotypically normal. No commonly misidentified lines were used in this study.

Cortical organoid and chimeroid differentiation

Dorsally patterned cortical organoids were generated following a protocol previously published by our group[7]. In brief, on day 0, feeder-free cultured human PS cells, 75–85% confluent, were enzymatically dissociated to single cells with Accutase (Gibco), and 9,000 cells per well were reaggregated in ultra-low-cell-adhesion 96-well plates with V-bottom conical wells (sBio PrimeSurface plate; Sumitomo Bakelite) using the same pluripotent cell medium in which they were previously maintained. At day 1, 80 µl of medium was replaced with cortical differentiation medium (CDM) I, containing Glasgow-MEM (Gibco), 20% knockout serum replacement (Gibco), 0.1 mM minimum essential medium non-essential amino acids (MEM-NEAA) (Gibco), 1 mM pyruvate (Gibco), 0.1 mM 2-mercaptoethanol (Gibco), with 1% of penicillin–streptomycin solution (Corning). From day 0 to day 6, ROCK inhibitor Y-27632 (Millipore) was added to the medium at a final concentration of 20 µM. Patterning small molecules, WNT inhibitor IWR1 (Calbiochem) and TGFβ inhibitor SB431542 (Stem Cell Technologies), were added from day 0 to day 18, at a concentration of 3 µM and 5 µM, respectively.

Single-donor and multidonor chimeroids were generated as previously described[9]. In brief, patterned EBs between day 15–18 were dissociated into single-cell suspensions using a modified papain-based protocol[9]. After confirming morphology, organoids were enzymatically and mechanically dissociated, then filtered and resuspended in CDM1 medium with ROCK inhibitor. Cell suspensions from different donors (in the case of multidonor chimeroids) were mixed in equal ratios and reaggregated (18,000–20,000 cells per well) in ultra-low-adhesion 96-well plates. Then, 2 days later, embryoid bodies were transferred to low-attachment dishes and cultured under orbital agitation. Medium was sequentially changed to CDM2, CDM3 (at DIV35) and CDM4 (at DIV70) as per established protocols[7]. For APM, organoids at day 70 were transferred into a medium containing BrainPhys Basal (Stem Cell Technologies), 20 ng ml^{-1} N2 supplement (1×, Thermo Fisher Scientific), 20 ng ml^{-1} B27 supplement (1×, Thermo Fisher Scientific), 1% penicillin–streptomycin solution 100× (Corning), 1% MEM-NEAA (Gibco), 1% GlutaMax (Gibco) and amphotericin B (Thermo Fischer Scientific). After filtration, GDNF and BDNF at a final concentration of 20 ng ml^{-1} were added. Along with dCAMP (MilliporeSigma), ascorbic acid (StemCell Technologies) and laminin (Thermo Fischer Scientific) at a concentration of 1 mM, 200 nM and 1 µg ml^{-1}. Half of the medium was replaced with fresh medium twice per week. Heterochronic and monochronic cultures were obtained using the previously described chimeroid strategy; however, papain dissociation time and mechanical dissociation were adjusted based on organoid age (25 min for younger organoids; for older organoids, mincing with a blade followed by 45 min of digestion). While the chimeroid strategy is extremely efficient in younger organoids, the success rate of the heterochronic cultures remains very low. This is probably due to the dual requirement for sufficient patterning in the young organoids and adequate stemness in the older cells, both of which are necessary to ensure robust signalling from the young tissue and sufficient recovery of older cells for analysis at day 14 after mixing. Chimeroids derived from old organoids were smaller than those derived from young organoids, probably due to the limited proliferative potential of the old neural progenitors. Organoid time-series include at least $n = 6$ organoids/3 batches at all stages (6 months to 5 years).

Mouse experiments

We used wild-type CD1 and C57BL/6 mice (Charles River Laboratories). Pregnant dams were euthanized to obtain embryos. Embryos were staged carefully according to Theiler stages for E11.5 and the neocortex was dissected. Stage-matched embryos were pooled (15–20 per experiment) prior to dissociation. The dissociation protocol described for the human chimeroids was used with some modifications. Dissociated progenitors were seeded to aggregate overnight at a density of 12,000 cells per well. The next day, the medium was switched to CDM2 for 3 days. On day 4 after seeding, the medium was changed to CDM3 and then to CDM4 on day 6. We quantified the number of nuclei with positive SATB2 expression across three condition groups: monochronic (old), monochronic (young) and heterochronic from cultures 1 day (D1AM; for each group: $n = 3$ replicate organoids × 3 batches) and 2.5 days (D2.5AM; for each group: $n = 3$ replicate organoids × 1 batch) after mixing, respectively. For evaluating the overall effect of condition on the proportion of nuclei with positive SABT2 expression at D1AM, binomial generalized

linear models (GLMs) were used to model the number of SATB2-positive nuclei out of total nuclei per organoid and adjust for batch by including batch as a fixed effect. Models with or without adding a condition as a fixed effect were evaluated by a likelihood ratio test using the anova function. Following the observation of the global effect of the condition being statistically significant (ANOVA, $P < 0.05$), estimated marginal means for each group were derived from the fitted full binomial GLM by using the R package emmeans, and Tukey-adjusted pairwise comparisons were performed between groups. For D2.5AM, due to the absence of more than one batch level to adjust for, we proceeded with computing estimated marginal means and performing pairwise comparisons between groups.

To fluorescently label neurons, we incubated cells while aggregating with AAV particles encoding GFP under the CAG promoter. The AAV serotype PHPeB permits efficient transduction of the central nervous system[36]. Organoids were fixed and imaged around 3weeks after aggregation on the LSM900 microscope. Images were acquired using the Zeiss microscope and processed in ImageJ (v.2.14.0/1.54 f). pAAV-CAG-GFP was acquired from Addgene (Addgene, 37825).

Statistical analysis

Organoids used for analysis or treatment were chosen from each batch to be representative of the morphology seen in that differentiation. For every experiment, organoids were collected without a preconceived selection strategy or priority. The investigators did not use blinding in this study. However, our analytical pipeline for each experiment followed uniform criteria applied to all samples, allowing us to analyse our data in an unbiased manner. All bioinformatics analyses were applied uniformly to all samples without considering genotype adjustments. Sample size was not predetermined using specific methods. At least three organoids were used for each experiment, guided by analysis from previous published work[6,7,30]. This prior research demonstrated the reproducibility of this organoid system and confirmed that using three organoids adequately captured variation.

Fixation and processing of samples for cryosectioning

Organoids were fixed in 4% paraformaldehyde (PFA) (Electron Microscopy Services) overnight in a 12-well plate (Falcon) at 4 °C, washed three times with 1× PBS (Gibco), and cryoprotected in a 30% sucrose solution (Sigma-Aldrich) in PBS overnight at 4 °C.

Gelatin solution containing 10% bovine gelatin (Sigma-Aldrich) and 7.5% sucrose (Sigma-Aldrich) was prewarmed at 37 °C for 15 min. The 30% sucrose solution was removed from the samples and exchanged for the prewarmed gelatin, and the samples were incubated at 37 °C for 15 min. Meanwhile, plastic moulds were coated with a 2 mm layer of warm gelatin solution and left to polymerize at room temperature. The samples were then transferred to the pretreated plastic moulds, and 1 ml of warm gelatin solution was added on top. After polymerization at room temperature for 3 min, the samples were prechilled at 4 °C for 15–20 min. Finally, the moulds were frozen in a cold bath containing 100% ethanol and dry ice for 2–3 min, and stored at −80 °C indefinitely.

Immunohistochemistry

For immunohistochemistry, 14–18 µm-thick sections were cut using the cryostat (Leica). Cryosections were stabilized at room temperature for 5 min and blocked with 10% donkey serum (Sigma-Aldrich) + 0.3% Triton X-100 (Sigma-Aldrich) in PBS. Primary antibodies (Supplementary Table 15) were diluted in the blocking solution and incubated overnight. After four washes with PBS, cryosections were incubated at room temperature with secondary antibodies diluted in PBS (1:1,000; Supplementary Table 15) for 1 h at room temperature, washed four times with PBS and stained with DAPI (1:10,000 in PBS + 0.1% Tween-20) for 5 min to visualize cell nuclei. At later timepoints (>1 year), we consistently observed a reduction in staining specificity, with increased background signal that limited reliable interpretation of most antibodies, despite extensive optimization. For the 2–3 year organoid immunohistochemistry, we used the fresh-frozen protocol described below.

Immunohistochemistry on fresh-frozen sections

Human brain organoids aged 2 to 5.8 years were rinsed with PBS, directly embedded in OCT compound (NEG-50, Richard-Allen Scientific) and then quickly frozen. Fresh-frozen OCT blocks were cryosectioned at 10 µm thickness. The sections were thawed onto Superfrost Plus Gold glass slides (EMS). Organoid depths of 0–150 µm were collected as serial sections. Sections were fixed in ice-cold methanol at −20 °C for 20 min, then rinsed with PBST0.1 (1× PBS with 0.1% Tween-20). Permeabilization was performed with PBST0.25 (1× PBS with 0.25% Tween-20) for 15 min. Blocking was done with 5% donkey or goat serum in PBST0.5 (1× PBS with 0.5% Tween-20) for 30 min. Alexa-Fluor-conjugated antibodies (NEUN/RBFOX3; 608455, BioLegend) were diluted 1:200 in blocking buffer and incubated with sections for 1–2 h. The sections were rinsed with PBST0.1 and incubated with 0.2 µg ml^{-1} DAPI for 3 min, then rinsed with PBS and water. ProLong Gold anti-fade mounting medium was applied, and coverslips were mounted. Images were acquired using LSM900 with Zeiss software. Image processing was done using ImageJ (v.2.14.0/1.54f). NeuN-positive nuclei were observed up to approximately 80 µm deep, beyond which they were not observed.

Hypoxyprobe assay

Hypoxyprobe (pimonidazole HCl; Hypoxyprobe Kit HPI-100) was applied to $n = 3$ 1-year-old CDM4 organoids at a final concentration of 100 µM. Organoids were incubated with the probe for 1.5 h at 37 °C and 5% CO_2. Samples were then washed with PBS, fixed in 4% PFA at room temperature for 2 h, embedded and sectioned at 14 µm. Immunohistochemistry was performed according to the manufacturer's instructions, and the primary antibody included in the kit was used at a 1:50 dilution[6].

Whole-organoid immunofluorescence

Organoids were washed in wash buffer (PBS with 0.4% BSA) and fixed at room temperature for 30 min with 4% PFA. After fixation, organoids were stored in 1× PBS with 0.1% Tween-20 (P9416, Sigma-Aldrich). Permeabilization, blocking and staining were performed as previously described[41]. Nuclei were counterstained with 0.5 µg ml^{-1} DAPI for 30 min. Organoids were optically cleared using RIMS and mounted as previously described[41,42]. Images were acquired with LSM880 (Zeiss) and LSM900 (Zeiss) using a ×40 objective. Images were processed with ImageJ (v.2.14.0/1.54f). Nuclei were segmented and quantified using ZEN blue v.3.1 Image Analysis and Intellesis software packages. Image segmentation was achieved using a previously trained ZEN Intellesis algorithm[43]. SATB2 intensity was thresholded to define positive nuclei and counted across the various *z*-stacks of individual organoids.

Microscopy

Immunofluorescence images were acquired using the Zeiss Axio Imager. Z2 with a ×20 objective (pixel size, 0.325 µm) using the Apotome optical sectioning function. The Zen Blue software was used to perform tile stitching and apotome deconvolution before exporting the images. For the LSM900, *z* stacks with 3 µm step size were acquired with a ×20 objective (pixel size, 0.62 µm), followed by tile stitching using the Zen Blue software. Further processing, such as *z* projections, channel merging and adding scale bars, was performed in Fiji v.43. Images were adjusted for brightness and contrast; all adjustments were applied to the whole image.

SATB2 and FOS quantification. Nine-month-old organoids from three genetic backgrounds (H1, PGP1 and 11a) were analysed ($n = 3$ organoids per condition per line; APM and CDM4). Three regions per organoid were randomly selected based on DAPI signal and imaged from three sections on the same slide. *z*-Stacks were acquired using a 20× objective

(0.62 µm per pixel; 3 µm step size; 3–5 optical sections) on a Zeiss system (Zen Blue). Acquisition settings were as follows: SATB2 (650 V, 2%, 28 µm pinhole), FOS (750 V, 10%, 31 µm) and DAPI (650 V, 1%, 27 µm). Stacks were converted to average-intensity projections and quantified in Fiji (v.43). SATB2-positive cells were defined as DAPI-positive nuclei with elevated SATB2 signal and were subsequently assessed for FOS expression.

Bulk RNA-seq from organoids

Snap-frozen organoids were resuspended in RLT buffer containing β-mercaptoethanol, and RNA was isolated with a DNase digestion step according to the manufacturer's protocol (RNeasy, Qiagen). Then, 10 ng of RNA was used for library preparation with the Smart-Seq Pico input total RNA library preparation kit, including ZapR depletion (with unique molecular identifiers (UMIs)), according to the recommended protocol. Libraries were quantified, pooled and sequenced on the NextSeq 2000 (Illumina) instrument.

DNA extraction and methylome analyses

Genomic DNA extraction and WGBS. Genomic DNA was isolated from organoids using a previously described method[44]. In brief, organoids were thawed on ice and suspended in 500 µl of resuspension buffer (240 µl of genomic lysis buffer (D4075, Zymo), 20 µl of proteinase K (D4075, Zymo) and 240 µl of nuclease-free water). The sample was thoroughly mixed, vortexed and incubated at 55 °C for 4 to 7 h at 300 rpm. An equal volume of phenol:chloroform:isoamyl alcohol (15593031, Thermo Fisher Scientific) was added, mixed by inversion and then centrifuged at 13,000*g* for 5 min. The aqueous phase (around 400 µl) was transferred to a new tube for precipitation. To this aqueous phase, 8 µl of Glycogen-Blue (AM9515, Thermo Fisher Scientific), 20 µl of 5 M NaCl (AM9760G, Thermo Fisher Scientific) and 1 ml of ethanol (E7023, Sigma-Aldrich) were added, mixed by inversion, and allowed to precipitate overnight at −20 °C. The tubes were spun at 13,000*g* for 45 min at 4 °C. The supernatant was discarded and 1 ml of 70% ethanol was added to the pellet, which was then spun down at 13,000*g* for 45 min at 4 °C. The supernatant was discarded, and the pellet was air-dried for 10 min before being resuspended in elution buffer (low-EDTA TE pH 8, 15575020, Thermo Fisher Scientific) and incubated at 55 °C for 10 min.

Genomic DNA was fragmented in a tube (MicroTube AFA Fiber pre-slit snap-cap 6 × 16 mm, 520045, Covaris) using a Covaris S-series S2 Sonicator with the following settings: duty cycle, 10%; intensity, 5; cycles per burst, 200; maximum temperature, 7 °C; duration, 76–90 s. Fragmented DNA was purified and concentrated using the DNA Clean & Concentrator kit (D4013, Zymo) and eluted in 22 µl of low TE (pH 8). 1 µl of the eluate was used for quality control on the Agilent TapeStation (HSD5000), resulting in an average fragment size of 237–322 bp. Bisulfite conversion was performed using the EZ DNA Methylation-Gold kit (D5005, Zymo), with the final converted DNA eluted in 16 µl of low TE (pH 8). Libraries were prepared using the xGen-Methyl-Seq DNA Library prep kit (10009824, IDT), in combination with xGen UDI Primer Plate 2 (8 nucleotides, 10009816, IDT). The number of PCR cycles used was 7. Each library underwent two final rounds of purification using AMPure XP beads (A63881, Beckman Coulter). Libraries were assessed for concentration, fragment size distribution and primer-dimer absence using the Agilent TapeStation (HSD5000). Sequencing was conducted on the Illumina NovaSeq 6000 and Element Biosciences Aviti platform, generating 150 base paired-end reads, targeting 800–900 million reads per sample.

WGBS processing. Raw reads were subjected to adapter and quality trimming using cutadapt[45] (v.4.6; parameters: --quality-cutoff 20 --overlap 5 --minimum-length 25; Illumina TruSeq adapter clipped from both reads), followed by trimming of 10 and 5 nucleotides from the 5′ and 3′ end of the first read and 15 and 5 nucleotides from the 5′ and 3′ end of the second read. Trimmed reads were aligned to the human reference genome (hg19) using BSMAP[46] (v.2.90; parameters: -v 0.1 -s 16 -q 20 -w 100 -S 1 -u -R). In this study, we used hg19 (rather than the current hg38) as the reference genome to maintain compatibility and coordinate consistency with previously generated reference datasets, annotation resources and downstream comparative analyses incorporated into our methylation analysis pipeline, including publicly available developmental brain methylation datasets and established epigenetic clock resources. Importantly, all samples and comparative analyses were processed uniformly within the same reference framework. Because our analyses focused primarily on genome-wide and regional DNA methylation patterns rather than fine-resolution structural variation or novel genomic annotations, we do not expect the use of hg19 versus hg38 to materially affect the biological conclusions of the study. Sorted BAM files were generated and indexed using samtools[47] with the 'sort' and 'index' commands (v.1.21). Duplicates were removed using the MarkDuplicates command from GATK (v.4.5.0.0; --VALIDATION_STRINGENCY = LENIENT --REMOVE_DUPLICATES=true --COMPRESSION_LEVEL 4 --ASSUME_SORT_ORDER coordinate)[48]. Methylation rates were called using mcall from the MOABS[49] package (v.1.3.9.6; default parameters; --reportCpX A/C/T for non-CpG methylation calling). All methylation analyses were restricted to autosomes and only CpGs covered by at least 10 and at most 150 reads were considered for downstream analyses. Assessment of global, genome-wide methylation was performed using average (arithmetic mean) methylation levels. Region-specific methylation was assessed by calculating average methylation levels across features (bins, partially methylated domains, highly methylated domains, DMVs, repeats, cdDMRs, superenhancers) using bigWigAverageOverBed from UCSC tools for each sample, where a feature was only considered if at least three CpGs were contained measurements within a region.

Endogenous comparison. cdDMRs defined from postnatal human brain were obtained from ref. 14. cdDMR coordinates in hg19 and their cluster assignment based on cell-type-specific methylation trajectories (six clusters: 1:G−N+, 2:G0N+, 3:G0N−, 4:G+N0, 5:G+N−, 6:G−N0) were used as provided by the study. cdDMRs were scored for mean methylation in organoid samples using bigWigAverageOverBed as described above (≥3 CpGs covered). To quantify recapitulation of temporal methylation dynamics in organoids, for each cdDMR, a linear regression model was fitted predicting mean cdDMR methylation from time in culture (in months), yielding a slope estimate (change in methylation per month). cdDMRs were classified as showing temporal changes over time in organoids if the absolute slope value had a minimum of 0.1/60 (corresponding to a predicted minimum change of 0.1 in methylation rate over 60 months). The fetal brain DNAm age was estimated using the FetalClock function from ref. 18, based on the implementation provided at GitHub (https://github.com/LSteg/EpigeneticFetalClock).

Differential methylation analysis. DMRs were called using metilene[50] (v.0.2-8). DMRs were defined by an absolute minimum difference in methylation of 0.1 with a maximum distance of 300 nucleotides between CpGs within a DMR and a minimum of 10 CpGs per DMR and Bonferroni correction for multiple testing (parameters: --m 10 --c 1 --d 0.1) and filtered by $q < 0.05$. DMRs were classified as hypo-DMRs and hyper-DMRs based on the direction of change. DMRs were associated with CGIs and DMVs based on a minimum overlap of 1 bp. DMRs were annotated to the nearest genes using GREAT[51] (v.4.0.4; default parameters).

To identify temporal changes in methylation, DMRs were called between early and late culture timepoints (3 months versus 5 years). DMRs were filtered to retain only those with a minimum absolute Pearson correlation coefficient of 0.6 between time in culture (in months) and mean DMR methylation rate across all timepoints.

To evaluate effects of APM on the methylation landscape, DMRs were called between organoids cultured for 9 months or 1 year in CDM4 and organoids cultured for 9 months or 1 year in APM.

Genomic feature annotation. CGIs were obtained from the UCSC Genome Browser (https://genome-euro.ucsc.edu/cgi-bin/hgTables).

CpG shores were defined as 2 kb regions flanking CGIs upstream and downstream; shelves were defined as 2 kb regions flanking the shores.

DMVs were defined based on WGBS data from the HUES64 human embryonic stem cell line[52]. To identify DMVs, a previously described sliding-window approach was adapted[53]. In brief, 5 kb windows with a 1 kb step size were generated across autosomes using bedtools[54] makewindows. Average CpG methylation was calculated for each window, excluding CpGs located within CGIs, and separately for CGIs. Windows and CGIs with an average methylation below 0.15 and containing at least 10 CpGs were merged, excluding regions composed solely of CGIs.

Annotations of highly methylated domains and partially methylated domains were obtained from GitHub (https://zwdzwd.github.io/pmd)[55].

Repeat annotations were obtained from the hg19 UCSC RepeatMasker track, excluding entries on alternative haplotypes, fix patches and chrMT.

Epigenetic clocks. CpG methylation values at low-coverage sites (coverage < 5) were imputed using the boostme package (v.0.1.0). Imputation was performed on individual samples represented as objects from the bsseq package (v.1.40.0). Imputed values exceeding one were capped at one. Array-based probe IDs were mapped to genomic coordinates using the Illumina EPIC array manifest (EPIC.hg19.manifest). The pan-tissue human methylation clock[17] was applied using the DNAmAge function from the methylclock[56] package (v.1.10.0). Cortical DNA methylation age[57] was estimated using the CorticalClock function based on the implementation provided at GitHub (https://github.com/gemmashireby/CorticalClock). DNAm age was assessed by the median absolute error between the time in culture of the organoids and the predicted methylation age in months, as well as Pearson correlation between the two across all samples.

To assess mitotic history, DNA methylation at solo-WCGW CpGs, which are particularly susceptible to methylation loss with cell division[55], was quantified. Methylation was evaluated across three feature sets: all solo-WCGWs, solo-WCGWs within common PMDs and solo-WCGWs in common PMDs represented on the HM450 array. Annotations were obtained from https://zwdzwd.github.io/pmd, and the average methylation levels across feature sets were calculated per sample from non-imputed WGBS data.

mCA. Forebrain superenhancers were obtained from a previously published dataset of fetal human brain tissue and cerebral organoids[15]. The mean mCA levels at these regions were compared with the background levels calculated across genome-wide 30 kb bins (approximating the average superenhancer size), excluding bins overlapping with superenhancers.

Locus methylation trend plots. For regions of interest (ROIs), the mean methylation was computed using bigWigAverageOverBed as described above (≥3 CpGs covered) and modelled as a function of time in culture (in months) using linear regression. Trends were visualized using per-ROI scatterplots with fitted regression lines (and 95% confidence intervals) and Pearson correlation estimates.

Visualizations. Unless stated otherwise, all statistics and plots were generated using R v.4.4.1. Violin plots were generated using the vioplot (v.0.5.1) or ggplot2 (v.3.5.2) package and show the kernel density estimation with embedded box plots indicating the median, interquartile range and whiskers extending to 1.5× the interquartile range. Circos plots were created using the RCircos (v.1.2.2) package from tracks with averaged profiles over 50 kb bins created using UCSC tools bigwigAverageOverBed. The differential signal was obtained by subtracting the 5-year profile from the 3-month profile. Cytoband and ideogram data for hg19 were obtained from the RCircos package. DMR methylation heat maps and average tracks were created using the EnrichedHeatmap[58] package (v.1.34.0) by applying the normalizeToMatrix function first, with 2,500 bp extensions up- and downstream and a target ratio of 0.4. Pairwise genome-wide correlations of methylation rates between samples of consecutive timepoints were plotted using the smoothScatter function. The box plots show the median (centre line), interquartile range (box) and the whiskers extend to 1.5× the interquartile range; individual observations are overlaid as points. Bar plots, box plots, scatter plots and line plots were created using ggplot2.

Electrophysiological analyses

Electrical signals were recorded using the Accura 3D CMOS-HD-MEA system by 3Brain (BioCAM DupleX system, in combination with Accura 3D chips). The 3D chip contains 4,096 penetrating μNeedle electrodes with 90 μm height arranged in 64 × 64 grid in a square measuring 3.8 × 3.8 mm, with a sampling rate of 20 kHz and a 12-bit resolution. CDM4 organoids were changed to APM medium 14–21 days before recording, and acute recordings from intact organoids were performed at 37 °C in a mini-incubator box filled with Carbogen. BrainWave v.5 was used to record spontaneous activity for 15–20 min. To test whether the electrical activity measured was synaptic, NMDA and AMPA receptor activity was blocked at the end of recordings using D-AP5 (150 μM) and DNQX (30 μM), respectively. Moreover, action potentials were blocked by bath application of TTX (1 μM). Spike detection was carried out by Kilosort2[31], followed by analysis of the spike train using custom MATLAB scripts (v.24.1, R2024b, The MathWorks). The detection of rapid spiking periods (burst) was performed by implementing the maximum interval[59] algorithm (maximum interval = 170 ms, maximum end interval = 400 ms, minimum interval between bursts = 800 ms, minimum duration of burst = 40 ms, minimum number of spikes = 4). The analysis of network bursting was performed on the basis of the population-averaged spiking rate along all detected units. A peak in the population signal was considered to be a network burst if it met the following criteria: (1) the peak amplitude was greater than 4× the s.d. of the noise value; (2) a set of bursting cells composed of at least 20% of total cells were active during that population spike; and (3) a cell was considered part of the set of bursting cells only if it participated in at least 50% of the network bursts. The peaks of the network bursts were used to measure the interburst interval (IBI), and the network burst rate was obtained from the average IBI. For organoids that displayed no bursts or networks bursts, the amplitude and duration values were imputed as 0. Outlier datapoints were identified and removed using the ROUT method (GraphPad Prism 10.5.0) with $Q = 0.1\%$.

EM analyses

A total of 18 organoids (three organoids per condition at 6 months: two H1 and one 11a genetic background, six organoids per condition at 12 months for both CDM4- and APM-treated conditions) were immersion-fixed in 2% PFA (EMS, 15710), 2.5% glutaraldehyde (EMS, 16220) and 0.003 M $CaCl_2$ (Sigma-Aldrich, C4901) in 0.1 M sodium cacodylate buffer (caco buffer, Sigma-Aldrich, C0250) for 48 h (at room temperature for the first 24 h and at 4 C for the remaining 24 h). Organoids were prepared for EM by treating them with 1% OsO_4 (EMS, 19170) with 10 mg ml^{-1} potassium ferrocyanide (EMS, 20150) and 0.003 M $CaCl_2$ in 0.1 M caco buffer for 1 h at room temperature. Organoids were washed afterwards and stained with a 2% OsO_4 solution with 0.003 M $CaCl_2$ in 0.1 M caco buffer for 1 h at room temperature. The sections were then stained with 2% uranyl acetate (EMS, 8473) at 4 °C overnight, dehydrated and embedded in LX-112 epoxy resin (LADD Research Industries, 21310) at 60 °C for 72 h. Blocks were trimmed and sectioned at 40 nm slice thickness with a Leica EM UC6 Ultramicrotome and sections were collected on carbon-coated Kapton tape using an automatic tape-collecting ultramicrotome[60]. Strips of tape were mounted onto silicon wafers and sections were post-stained with 2% uranyl acetate in water and 3% lead citrate (Leica Biosystems ULTROSTAIN II). Sections were imaged using a FEI Magellan scanning electron microscope (Thermo Fisher Scientific) equipped with a custom image acquisition software (WaferMapper)[61]. A total of 12 panoramic high-resolution images (one per organoid) were acquired using the backscattered electron detector (7 kV, 1 μs per pixel dwell time, ranging from 86,000 to 106,000 pixels in the x axis and from 106,000 to 150,000 pixels in the y axis, at

4 nm resolution). Owing to natural size variation among organoids, the final 2D panoramas varied slightly in dimensions to ensure spatial coverage from the surface to the central region of each organoid. Stitched EM images were imported into VAST[62] for visualization and manual annotation of synaptic clefts, creating a ground-truth dataset. A deep neural network based on a U-Net architecture[63] was then trained on this ground truth using the mEMbrain MATLAB package[21]. The annotated dataset comprised less than 5% of the total volume and was produced by two human experts (around 20 h total annotation time; pixel-level validation accuracy > 0.95). mEMbrain's interactive environment facilitated both model training and accuracy evaluation. Predicted synapses were represented as 2D probability maps registered to the EM images in VAST. Synapses were initially defined as connected components of pixels with a synapse probability greater than 40%, a threshold chosen to approximate expert annotations. Model performance exceeded 95% accuracy based on manual verification of the largest synapses (>95th percentile by area), providing an estimate of the false-positive rate for unbiased condition comparisons. To standardize automatic synapse quantification across sections, a computational synapse-size threshold was determined for each section individually. Specifically, 103 randomly selected predicted synapses per section were manually classified as synapse or non-synapse by a human expert. A psychometric curve was then fitted to these annotations to establish a threshold corresponding to over 80% model accuracy. Final synapse counts per section were obtained using these individualized thresholds, ensuring objectivity and consistency across samples. To account for structural variability and region-specific differences in synapse distribution, each section was divided into five horizontal segments. Synaptic density was calculated in each segment, and the one with the highest density was selected for statistical comparison (within each section, synaptic density variation across segments ranged from 0.00 to 0.14). This approach minimized sampling bias across organoid layers. The same set of 103 randomly selected predictions was further used to classify synaptic contacts by their postsynaptic target. Synapses were categorized as spine synapses if they were located on putative dendritic spines—morphologically consistent with spine-like structures observed in 2D EM—or on clearly defined spines attached to dendritic shafts. The remaining synapses were classified as targeting non-spine elements. Comparisons of synaptic densities across groups were performed using the Wilcoxon rank-sum test. The distribution of spine versus non-spine synapses was analysed using two-sided Fisher's exact tests. Statistical significance was defined as $P < 0.05$.

Expansion microscopy analyses

We adapted a recent approach leveraging expansion microscopy and combinatorial antigen barcoding[26]. Seven-month-old organoids cultured in either CDM4 or APM were transduced with a mix of nine AAVs (8×10^8 viral genomes each), each expressing a CAG-driven spaghetti-monster fluorescent protein[27] tagged with distinct epitopes (V5, MYC, Flag, Ollas, E, S, HSV, protein C or Ty1). After 3 weeks, organoids were fixed in 4% PFA, embedded in gelatin, cryosectioned at 50 µm and mounted on HistoBond slides. The sections were expanded using the Magnify protocol[28], including methacrolein anchoring, overnight gelation at 37 °C, sample homogenization and expansion through water washes. Fully expanded samples were re-embedded in a non-expandable hydrogel to allow iterative immunostaining. Re-embedded samples were blocked and stained with primary antibodies overnight, washed and incubated with secondary antibodies the following night. For multiround immunostaining, antibody destaining was performed under the same homogenization conditions used for the initial sample preparation. Before imaging, samples were transferred to six-well glass-bottom plates. A Nikon W1-SORA spinning-disk confocal microscope was used: ×4 overview images identifying dense regions were followed by ×10 *z* stacks and ×40 tile scans. Large ×40 scans were stitched using BigStitcher; registration across rounds was performed with BigStream using a two-stage alignment pipeline (coarse RANSAC-based feature matching, followed by fine intensity-based registration using mutual maximum information). Affine transformation matrices were applied to full-resolution datasets. Preprocessing for low-signal-to-noise-ratio rounds included percentile-based contrast enhancement and 3D median filtering. Aligned volumes were converted to .wkw format, imported into Webknossos and merged into a single nine-channel dataset. Ten neurons per sample (CDM4, APM) were manually skeletonized based on multitag expression in the cytosol. Resulting traces (30 per condition) were converted to .swc files, and morphometric parameters were quantified using Navis in Python. In the Strahler analysis of CDM4 and APM neurons, terminal branches receive Strahler number one. When two branches with the same Strahler number meet at a branch point, the Strahler number of the next segment increases by one.

Dissociation of brain organoids and scRNA-seq

Organoids were dissociated as previously described[9]. Dissociated cells were resuspended in 100 µl of PBS, filtered with a 35 µm cell strainer tube (Corning) to remove aggregates and counted with a Countess II automated haematocytometer (Thermo Fisher Scientific) or a Cellometer K2 (Nexcelom Bioscience) and AOPI stain (Nexcelom Bioscience, CS2-0106-5ML). Single-cell suspensions were loaded into the Chromium Next GEM Chip G (10x Genomics, 1000120) and run with the Chromium Controller to generate single-cell GEMs. scRNA-seq libraries were prepared with the Chromium Single Cell 3′ Library and Gel Bead Kit v3.1 (10x Genomics, 1000268). The resulting libraries were pooled based on molar concentration and sequenced on a NovaSeq X or NovaSeq 6000 instrument (Illumina) either 28 bases for read 1, 55 bases for read 2 and 8 bases for index read 1, or 28 bases for read 1, 90 bases for read 2 and 10 bases for index read 1 (Supplementary Table 1). If necessary, after the first round of sequencing, we repooled libraries based on the actual number of cells in each library, and resequenced with the goal of producing an equal number of reads per cell for each sample (with a target read depth of 20,000 reads per cell).

scRNA-seq data analysis

The preprocessing of all scRNA-seq samples, including the conversion of raw BCL files into FASTQ files, reads alignment, and the generation of gene-barcode matrices, was performed using 10x Genomics Cell Ranger suite tool[64] following the steps described in our previous publication[9]. For de novo generated samples with moderate to high ambient RNA levels, CellBender[65] v.0.3.0 was used to remove systematic biases and background noises (Supplementary Table 1). The remove-background pipeline with the default parameters was used by taking the raw gene-by-cell count matrices produced by Cell Ranger pipelines as inputs. The filtered gene–barcode count matrices generated by Cell Ranger and CellBender were imported into Seurat (v.4.3.0)[66] for downstream analysis.

Genetic demultiplexing. In the cases in which multiple samples of different genetic backgrounds were pooled together and sequenced in the same lane to maximize the sequencing capacity, Demuxlet (v.1.0)[67] was applied with default parameters to determine the sample identity for each barcoded droplet and identify ambiguous droplets and doublets that contain two heterogeneous cells. Ambiguous droplets and doublets identified were removed from downstream analysis. To run Demuxlet, the BAM file output from Cell Ranger, the filtered barcode list generated by the initial preprocessing pipeline and reference variant-call-format (VCF) files for each expected cell line were used as inputs. The reference VCF files were prepared according to the method described in our previous publication[9].

To address doublet overestimation when applying Demuxlet to multiplexed samples with ambient RNAs, after using CellBender, Souporcell (v.2.5)[68] was suggested by the developer and was used with default

parameters as an alternative method, which allows genotype-free demultiplexing and clusters cells by the genetic variants detected within the input reads. The same set of input data plus the GRCh38 human reference genome FASTA file were used. We followed recommendations to include the reference VCF that has genetic variants of pooled individuals to enhance accuracy. Lastly, the Assign_Indiv_by_Geno.R function from the Demuxafy[69] framework was used to correlate clusters with donors in the reference SNP genotypes.

scRNA-seq data quality control, normalization, dimensionality reduction and clustering. For each scRNA-seq dataset, we performed initial quality-control filtering and retained cell profiles with total UMI counts of greater than 500 and less than 20,000, unique feature counts greater than 200 and a percentage of mitochondrial RNA less than 15. Seurat's SCTransform function was used to normalize the data and regress out the mitochondrial RNA percentage. The RunPCA function was used to perform principal components analysis (PCA), and the top 30 principal components were used by the FindNeighbors function to construct a *k*-nearest-neighbour graph with the default parameters. Cells were then clustered by the Louvain algorithm using the FindClusters function with resolution = 0.3 for a rough granularity to start with. Clusters showing atypically low UMI counts, low unique feature counts and a high percentage of mitochondrial RNA were labelled as low-quality cells and removed (Supplementary Table 5).

Data compilation of group-published data. To unify data processing across datasets, raw scRNA-seq FASTQ files for organoids from refs. 6,7 were reprocessed using Cell Ranger v.7.2.0 (the most notable change from the original processing is the inclusion of intronic reads in the count matrices).

Cluster annotation and data integration. Before any data merging/data integration, for each scRNA-seq data, we manually annotated each cluster by an ensemble approach, as described in our previous publication[9]. Doing so provides a solid way for cell type assignments by taking the previous domain knowledge, Seurat's FindMarkers output and alignment with notations in previously published reference maps[6] into consideration.

In pursuit of comparing organoids cultured under the conventional CDM4 and the novel APM conditions, we profiled APM-treated organoids at 4 months, 6 months, 9 months, 1 year and 1.5 years in this study. To facilitate downstream comparative analysis and enable more interpretable results, we refined cell type annotations between treatment conditions and corrected for sequencing batches as follows: For each age, scRNA-seq datasets from two conditions were merged by using Seurat's merge function. Considering the notable data imbalance between CDM4- and APM-treated organoids at 4 months and to control the overall cell number disparity between conditions, a 50% downsampling was applied on the CDM4 scRNA-seq dataset while retaining the original sample proportions before merging. Features that are repeatedly variable across datasets in the list were obtained by using Seurat's SelectIntegrationFeatures using the default parameters and were set as the variable features of the merged object. The RunPCA function was applied, and the merged data were then batch-corrected using Harmony[70] v.1.2.0. The downstream clustering used the standard Seurat pipeline by taking Harmony-corrected embeddings with a resolution set between 0.8 and 1.0. To examine the top upregulated genes within each cluster for cell type annotation, before using FindAllMarkers, Seurat's PrepSCTFindMarkers was used to recalculate the SCT assay by taking the minimum median UMI across all datasets being merged as a scale factor to correct for sequencing depth variations across different datasets. To achieve higher resolution and finer granularity in certain clusters, including clusters that were labelled as cycling cells and clusters with underlying heterogeneity of cell types, subclustering was performed (Supplementary Table 5). Although the neuronal cluster identified at 5 years contained both cells expressing inhibitory markers and cells expressing excitatory markers, due to the small size of this cluster (101 cells), we did not attempt further subclustering. Owing to the absence of organoid samples with matched genetic backgrounds across conditions, the integrated 4-month data were excluded from the age-wise comparative analysis across conditions. Thereby, we retained cell profiles from organoids with matched genetic backgrounds for other timepoints for data representation and downstream analysis as follows: 4 months (CDM4: $n = 6$, 15,972 cells; APM: $n = 2$, 4,579 cells), 6 months (CDM4: $n = 10$, 64,817 cells; APM: $n = 9$, 41,231 cells), 9 months (CDM4: $n = 6$, 18,104 cells; APM: $n = 3$, 8,533 cells), 12 months (CDM4: $n = 4$, 7,802 cells; APM: $n = 3$, 6,084 cells), 1.5 years (CDM4: $n = 2$, 3,952 cells; APM: $n = 2$, 8,670 cells).

To assess the reproducibility of organoids, we calculated Aitchison distances based on cell type compositional data between every unique pair of samples at each timepoint by using the aDist function from the R package robCompositions (v.2.3.1)[71]. Aitchison distances between replicates within the treatment protocol were compared by two-sided Wilcoxon rank-sum tests. Five previously published human fetal cortex datasets[6,38,39], as noted in our previous publication[9], were used to provide referential median sample-to-sample variabilities by their respective cell type annotations. Samples from the combined perinatal datasets from the Kriegstein lab[10,11] were grouped by age range (fetal samples by gestational month, and postnatal samples into 0–1 year, 1–2 years and 2–4 years) so that the Aitchison distances were calculated only between samples at similar ages.

To obtain a comprehensive overview of the organoid development across timepoints, we generated a developmental time map by merging the annotated scRNA-seq data of CDM4-treated organoids, including 424,720 cells from 110 organoid samples across 15 days ($n = 1$; 8,831 cells), 23 days ($n = 6$; 29,769 cells), 1 month ($n = 6$; 37,876 cells), 1.5 months ($n = 6$; 35,898 cells), 2 months ($n = 6$; 37,194 cells), 3 months ($n = 31$; 69,719 cells), 4 months ($n = 6$; 33,825 cells), 5 months ($n = 6$; 32,115 cells), 6 months ($n = 12$; 74,172 cells), 9 months ($n = 10$; 32,550 cells), 12 months ($n = 4$; 7,802 cells), 1.5 years ($n = 6$; 8,515 cells), 24 months ($n = 4$; 11,228 cells), 36 months ($n = 2$; 2,481 cells), 42 months ($n = 2$; 691 cells) and 60 months ($n = 2$; 2,054 cells). In general, we annotated 23 cell types, and we grouped cell types into several populations for broader representation as follows: (1) progenitors (aRG, oRGs, IPs); (2) excitatory neurons (ExNeu) (CFuPNs, CPNs, unspecified projection neurons (PNs) and newborn deep-layer projection neurons (newborn DL PNs)); (3) interneurons (INT) (immature interneurons, interneuron progenitors); (4) glial progenitors (GlialProg) (glial precursors, tRGs); (5) astrocytes (AST); and (6) OPCs. All other annotated cell types were grouped as 'other'. Annotation of de novo generated datasets was performed manually, guided by the most current biological evidence from the literature and informed by our previously published findings. For the oldest organoid timepoints, where clusters were not always readily distinguishable based on canonical marker expression alone, annotations were assigned using an integrative approach that incorporated marker profiles, label transfer from earlier timepoints and biological judgment informed by the literature.

The merged data were jointly renormalized by SCTransform and reprocessed using the standard Seurat pipeline. The time-series object of APM-treated organoids from 4 months to 1.5 years was generated by the same method after merging the APM counterpart from age-wise integrated data as described above.

Analysis of previously published human fetal data. A combination of two previously published perinatal single-nucleus RNA-seq (snRNA-seq) datasets for human cortical development were used for comparison. The dataset from ref. 10 includes profiles from 709,372 nuclei of 169 brain tissue samples from 106 individuals, with a wide age range spanning from the second trimester of gestation to adulthood. The snRNA-seq data and metadata were downloaded from https://cells.ucsc.

edu/?ds=pre-postnatal-cortex. We subsetted the snRNA-seq data to an age range from the second trimester up to 4 years, which is a proxy for the time window in our time-series data. The data were further subset by brain regions including cortex and frontal cortex with a spectrum of cell type populations including progenitors, excitatory neurons, interneurons, glial progenitors, astrocytes and OPCs. The dataset was further downsampled to include a maximum of 10,000 nuclei from any given annotated cell type (as defined by the original authors) at any given age range (second trimester, third trimester, 0–1 year, 1–2 years or 2–4 years), yielding a final subset of 151,749 nuclei from 56 individuals. Samples from ref. 11 that had an estimated age of less than 100 post-conceptional days and came from cortex or prefrontal cortex regions were selected to be combined with the ref. 10 data. In total, 36,751 cells from 6 individuals met these criteria, and were merged with the above dataset. The combined reference, comprising 188,500 cells from 62 individuals, was collectively renormalized using Seurat's SCTransform function. To compare with the reference human perinatal snRNA-seq dataset and explore what age the time-series organoids data maps to, we used labels by concatenating the information of cell type classes and age and performed reference-based label transfer using Seurat's FindTransferAnchors and MapQuery functions.

Identification of MCPs associated with ageing. To explore the maturation profiles of the time-series organoids data, we used the aforementioned human perinatal dataset as inputs and applied DIALOGUE (v.1.0)[12], a tool designed to identify MCPs of co-regulated genes across different cell types and map how the transcriptome varies with changes in its environment. Following DIALOGUE's vignette, a list of cell type objects was generated by the make.cell.type function to represent major cell populations in the human perinatal dataset by using a series of input arguments including the single-cell gene expression data, sample identity and PCA embeddings for each cell type of interest. Metadata of the SCTransform-normalized total UMI counts and the developmental age in days were included as a technical variability and a meaningful biological covariate to adjust for the analysis. Next, the DIALOGUE.run function was applied to the above list. As a result, five MCPs were identified, and each MCP output cell-type-specific upregulated and downregulated gene sets. We ran Seurat's AddModuleScores function on the combined perinatal tissue reference, using each of DIALOGUE's MCP and cell-type-specific gene lists as inputs. For each MCP, we assigned an overall score to each cell by subtracting the module score calculated from the downregulated gene set that matched that cell's cell type from the score of the corresponding upregulated gene set. In perinatal tissues, of the five MCPs, MCP4 most consistently showed the highest correlation with age within most cell population and across all cells; we therefore focused on the cell-type-specific up-minus-down MCP4 module scores as maturation scores and we adopted the same approach to calculate the maturation scores by using the above master gene sets in the context of our 15-day to 5-year organoid timeseries dataset, our 4-month to 18-month APM versus CDM4 organoid dataset, and our human heterochronic and monochronic organoid datasets.

For scatter plot representations, the R geom_smooth() function was used to add smoothed conditional means (black lines) with default 95% CIs (grey regions). Points were given slight *x*-axis jitter to improve visibility; horizontal position within a timepoint does not indicate differences in age. Heat map representations were generated to show the expression of either all MCP4 genes (in organoids) or cell-type-specific MCP4 genes (within a given cell population in organoids), respectively, over time. Values for each timepoint represent the mean of the counts-per-million of the pseudobulked count matrices for either each organoid or a given cell type within each organoid of that timepoint, respectively. *z*-Score normalization was performed for each gene. Genes are ordered by the weighted expression over time, by positioning genes expressed mostly at earlier time points at the top, and genes expressed mostly at later time points at the bottom.

GSEA. To investigate and compare temporal changes of astrocytes in organoids and temporal changes of astrocytes in endogenous perinatal human cortex, differential expression analyses were first performed in each dataset, treating age as a continuous variable. All genes were ranked based on the significance and direction of change (using the negative-log-transformed *P* value multiplied by the sign of the log-transformed fold change as the ranking metric). The top 500 upregulated genes over time in perinatal tissue astrocytes and the top 500 downregulated genes over time (marked with vertical blue lines) were used as gene sets for Kolmogorov–Smirnov tests based on the ranking in organoids. For visualizing results, the running enrichment scores (*y* axis) are shown as red (for upregulated genes) and blue (for downregulated genes) curves, which track the cumulative walk down the ranked data by increasing/decreasing given the presence/absence of a gene in the target gene set. Maximum absolute values of the running enrichment scores are the Kolmogorov–Smirnov tests' *D* statistic. *P* values of the Kolmogorov–Smirnov tests are shown in boxed text. Identical analyses were performed by taking the endogenous tissue data as the rank data, and the top 500 up and downregulated genes as gene sets.

Analysis of presynapse, synapse and post-synapse signature modules. Gene sets of GO terms: synapse (GO: 0045202), presynapse (GO: 0098793) and post-synapse (GO: 0098794) containing 1,778, 879 and 1,181 genes, respectively, were retrieved from the SynGO knowledge base of release v.1.2 (https://www.syngoportal.org/)[72]. Each gene set was used to calculate module scores for cells in integrated scRNA-seq data of CDM4- and APM-treated organoids at 6 months, 9 months and 12 months using Seurat's AddModuleScore function. To compare, under each age, whether organoids under two treatment conditions displayed different averaged expression levels for each program, LMEMs were built by the R package lme4[73] to model the scores by including which organoid the cell belongs to and the genetic background of that organoid as random effects (score ~ (1|organoid) + (1|genotype)). To adjust for cell count differences in each broad cell population across organoids, the reciprocal of the square root of the observed cell count per population per organoid was included as a weight factor. Models with or without treatment as an additive fixed effect were compared by the anova function from the R stats package and *P* values across tests of the above three signature modules were adjusted using the Benjamini–Hochberg method.

Analysis of Hallmark apoptosis, hypoxia and glycolysis gene signatures. We used the R package msigdbr v.25.1.0 to access MSigDB Hallmark gene sets for apoptosis, hypoxia and glycolysis. Each of these gene sets was used as an input to Seurat's AddModuleScores function to assign scores to cells from our 15-day to 5-year organoid timeseries dataset, as well as to our 4-month to 18-month APM versus CDM4 organoid dataset. For each Hallmark module score, we used mixed-effects models through lme4 to assess whether there were significant changes over time, both globally (across all cell types) by comparing the model score ~ log(months) + (1|organoid) + (1|broad_cell_type) against a similar model but excluding a covariate for the age of the organoids. Similar tests were performed within each broad cell type independently (excluding the covariate for cell type, of course).

Comparing cell type proportions between treatment conditions. The cell type proportion changes between CDM4- and APM-treated organoids at 4 months, 6 months, 9 months, 1 year and 1.5 years were evaluated by NBME models. A matrix of cell counts for each annotated cell type per organoid was generated. Given a cell type of interest, a NBME model was created using the glmer.nb function from lme4[73], which takes the genetic background of an organoid replicate as a random

effect to account for the variability in genotypes. The model also includes the logarithm of the total cell number of each organoid sample as an offset to account for the cell count differences (model formula: cell type ~ offset(log(library size)) + (1|genotype)). The significance of cell type proportion differences between organoids under two treatment conditions was calculated by the one-sided likelihood ratio test comparing negative binomial models with and without treatment as an additive fixed effect using the anova function. The Benjamini–Hochberg method was used to adjust *P* values from multiple independent tests. Cell type proportion differences between MonChr chimeroids and 9 month organoids were calculated using the same methods as above and only considering cell types with a minimum abundance of 5% in 9 month organoids.

Comparing cell cycle proportions between treatment conditions. Following Seurat's vignette, we used the CellCycleScoring function to calculate G2M and S-phase module scores per cell in our APM versus CDM4 organoid dataset. Cells that scored below 0.1 in both G2M and S-phase modules were designate as non-cycling, and cells that scored 0.1 or higher in either module were designated as cycling. To test differences in the proportion of progenitors that are cycling between APM-treated and CDM4-treated organoids, we considered each type of progenitor cell independently, and we constructed binomial mixed-effects models vi lme4 with the design: cycling ~ months + treatment + (1|organoid), compared against a similar model excluding the covariate for treatment using the anova function.

DEG analysis and GO analysis. To identify differentially expressed genes (DEGs) between CDM4- and APM-treated organoids at each time point (6, 9 and 12 months), we used a pseudo-bulk approach to analyse the data at the sample level. We took pan-ExNeu, AST and IN as partitions of interest by using the above-mentioned grouping criteria. Pseudobulk profiles were generated on a partition basis by aggregating UMI counts for each gene across cells of that partition within each organoid sample. We require at least 20 cells within a partitioned cluster per organoid to retain the sample. Genes with fewer than ten total UMI counts in at least two samples were excluded. The pseudo-bulk differential expression analysis was performed by using DESeq2[74] with the design formula ~genotype + treatment to identify DEGs between treatment conditions while regressing out the variation by genetic backgrounds. DEGs were defined by a cut-off with the absolute value of $\log_2$-transformed fold change > 0.5 and FDR-adjusted $P < 0.05$. Upregulated DEGs were used by the enrichGO function from clusterProfiler[75] to perform GO enrichment analysis. The simplify function with a default similarity cutoff of 0.7 from the same package was used to remove the semantic redundancy of enriched GO terms.

Comparative analysis of DIALOGUE-determined maturation scores. To examine whether APM-treated organoids show different DIALOGUE maturation scores in a time-series or time-specific manner, the age-wise integrated data from 4 months to 1 year were merged and jointly renormalized by SCTransform and reprocessed by the standard Seurat pipeline. We used Seurat's AddModuleScore function to calculate module scores using the DIALOGUE MCP4 full list of 'up' and 'down' genes for each broad cell type, separately, and then took the subtraction of the corresponding cell type's 'up − down' for each cell as a single maturation score, as described above. For the comparative analysis, the *z* score, with a mean of 0, was used to represent the magnitude. Maturation module scores across the entire dataset were standardized using the R function scale. Focusing on the excitatory neurons, we first assessed the treatment effect over time by treating age as a continuous variable. The *z* scores were averaged across all cells within the partition of interest per organoid. A baseline linear model was created to evaluate how maturation scores change with age (score ~ age). A second linear model incorporating treatment in addition (score ~ treatment + age) was used to compare with the baseline model by anova function from the R stats package to test whether adding treatment as an additive effect significantly improves the model fitting. Next, to assess in a time-specific manner, LMEMs were used to model the scores by including which organoid the cell belongs to and the genetic background of that organoid as random effects (score ~ (1|organoid) + (1|genotype)) and a weight factor to adjust for cell count differences in excitatory neurons across organoids. Models with or without treatment as an additive fixed effect were evaluated by anova function. The above statistical models were built by the R lme4[73] package.

Confidence intervals. Throughout the text, 95% CIs for statistical tests were calculated using the confint function from the R stats package v.4.4.0, except in the case of the results from Fisher's exact tests, for which confidence intervals are reported directly from the outputs of the fisher.test function from the stats package.

Reporting summary

Further information on research design is available in the Nature Portfolio Reporting Summary linked to this article.

Data availability

Raw scRNA-seq data supporting the findings of this study are available at dbGaP (study accession number phs004871) along with processed data from one organoid from the CW50037 cell line. Raw data from four organoids from the Mito210 cell line cannot be publicly shared due to limitations of donor consent. Processed scRNA-seq data supporting the findings of this study are available at the Broad Single Cell Portal (SCP) (https://singlecell.broadinstitute.org, study ID SCP3697), and at the Gene Expression Omnibus (GEO) (GSE333707), with the exception of processed data from one organoid from the CW50037 cell line, which is included in the dbGaP submission due to limitations of donor consent, and four organoids from the Mito210 cell line, which cannot be publicly shared due to limitations of donor consent. Processed WGBS data supporting the findings of this study are available at the GEO (GSE333708). Raw WGBS data are available on request to the corresponding author. See also Supplementary Table 1. Previously published data supporting the findings of this study are available as follows: processed data from ref. 9 (Broad SCP, study ID SCP2609) and raw data from Synapse under accession number syn52132869). Processed data from ref. 6 are all available at the Broad SCP (study ID SCP1756) and raw data are available at Synapse under accession number syn26346373. Processed data from ref. 30 are available at the Broad SCP (study ID SCP1129) and raw data are available at Synapse under accession number syn26346373. Processed data from ref. 7 are available at the Broad SCP (study ID SCP282) and raw data can be accessed from the GEO (GSE129519). Processed data from ref. 10 are available from the GEO (GSE162170). Processed data from ref. 10 are available from the UCSC Cell Browser (https://cells.ucsc.edu/?ds=pre-postnatal-cortex+all+rna). Processed data from ref. 11 are available from the UCSC Cell Browser (https://cell.ucsf.edu/snMultiome). Postnatal DLPFC methylation data from ref. 14 are available from Synapse under accession syn5842535 (Supplementary Table 1).

Code availability

Code used during data analysis is available at GitHub (https://github.com/tfaits/Arlotta_Lab_LongTermOrganoids), with the exception of custom code used for MEA analysis, which is available on request.

40. Quadrato, G. et al. Cell diversity and network dynamics in photosensitive human brain organoids. *Nature* **545**, 48–53 (2017).
41. Grosswendt, S. et al. Epigenetic regulator function through mouse gastrulation. *Nature* **584**, 102–108 (2020).
42. Sampath Kumar, A. et al. Spatiotemporal transcriptomic maps of whole mouse embryos at the onset of organogenesis. *Nat. Genet.* **55**, 1176–1185 (2023).

43. Frey, E. C., Humm, J. L. & Ljungberg, M. Accuracy and precision of radioactivity quantification in nuclear medicine images. *Semin. Nucl. Med.* **42**, 208–218 (2012).
44. Haggerty, C. et al. Dnmt1 has de novo activity targeted to transposable elements. *Nat. Struct. Mol. Biol.* **28**, 594–603 (2021).
45. Martin, M. Cutadapt removes adapter sequences from high-throughput sequencing reads. *EMBnet J.* **17**, 10–12 (2011).
46. Xi, Y. & Li, W. BSMAP: whole genome bisulfite sequence MAPping program. *BMC Bioinform.* **10**, 232 (2009).
47. Li, H. et al. The Sequence Alignment/Map format and SAMtools. *Bioinformatics* **25**, 2078–2079 (2009).
48. McKenna, A. et al. The Genome Analysis Toolkit: a MapReduce framework for analyzing next-generation DNA sequencing data. *Genome Res.* **20**, 1297–1303 (2010).
49. Sun, D. et al. MOABS: model based analysis of bisulfite sequencing data. *Genome Biol.* **15**, R38 (2014).
50. Jühling, F. et al. metilene: fast and sensitive calling of differentially methylated regions from bisulfite sequencing data. *Genome Res.* **26**, 256–262 (2016).
51. McLean, C. Y. et al. GREAT improves functional interpretation of cis-regulatory regions. *Nat. Biotechnol.* **28**, 495–501 (2010).
52. Charlton, J. et al. TETs compete with DNMT3 activity in pluripotent cells at thousands of methylated somatic enhancers. *Nat. Genet.* **52**, 819–827 (2020).
53. Hetzel, S. et al. Acute lymphoblastic leukemia displays a distinct highly methylated genome. *Nat. Cancer* **3**, 768–782 (2022).
54. Quinlan, A. R. & Hall, I. M. BEDTools: a flexible suite of utilities for comparing genomic features. *Bioinformatics* **26**, 841–842 (2010).
55. Zhou, W. et al. DNA methylation loss in late-replicating domains is linked to mitotic cell division. *Nat. Genet.* **50**, 591–602 (2018).
56. Pelegí-Sisó, D., de Prado, P., Ronkainen, J., Bustamante, M. & González, J. R. methylclock: a Bioconductor package to estimate DNA methylation age. *Bioinformatics* **37**, 1759–1760 (2021).
57. Shireby, G. L. et al. Recalibrating the epigenetic clock: implications for assessing biological age in the human cortex. *Brain* **143**, 3763–3775 (2020).
58. Gu, Z., Eils, R., Schlesner, M. & Ishaque, N. EnrichedHeatmap: an R/Bioconductor package for comprehensive visualization of genomic signal associations. *BMC Genom.* **19**, 234 (2018).
59. Kirillov, A. *NeuroExplorer Manual* (Nex Technologies, 1998–2014).
60. Kasthuri, N. et al. Saturated reconstruction of a volume of neocortex. *Cell* **162**, 648–661 (2015).
61. Hayworth, K. J. et al. Imaging ATUM ultrathin section libraries with WaferMapper: a multi-scale approach to EM reconstruction of neural circuits. *Front. Neural Circuits* **8**, 68 (2014).
62. Berger, D. R., Seung, H. S. & Lichtman, J. W. VAST (Volume Annotation and Segmentation Tool): efficient manual and semi-automatic labeling of large 3D image stacks. *Front. Neural Circuits* **12**, 88 (2018).
63. Ronneberger, O., Fischer, P. & Brox, T. U-Net: Convolutional networks for biomedical image segmentation. In *Proc. Medical Image Computing and Computer-Assisted Intervention 2015* (eds Navab, N. et al.) 234–241 https://doi.org/10.1007/978-3-319-24574-4_28 (Springer, 2015).
64. Zheng, G. X. Y. et al. Massively parallel digital transcriptional profiling of single cells. *Nat. Commun.* **8**, 14049 (2017).
65. Fleming, S. J. et al. Unsupervised removal of systematic background noise from droplet-based single-cell experiments using CellBender. *Nat. Methods* **20**, 1323–1335 (2023).
66. Hao, Y. et al. Integrated analysis of multimodal single-cell data. *Cell* **184**, 3573–3587 (2021).
67. Kang, H. M. et al. Multiplexed droplet single-cell RNA-sequencing using natural genetic variation. *Nat. Biotechnol.* **36**, 89–94 (2018).
68. Heaton, H. et al. Souporcell: robust clustering of single-cell RNA-seq data by genotype without reference genotypes. *Nat. Methods* **17**, 615–620 (2020).
69. Neavin, D. et al. Demuxafy: improvement in droplet assignment by integrating multiple single-cell demultiplexing and doublet detection methods. *Genome Biol.* **25**, 94 (2024).
70. Korsunsky, I. et al. Fast, sensitive and accurate integration of single-cell data with Harmony. *Nat. Methods* **16**, 1289–1296 (2019).
71. Templ, M., Hron, K. & Filzmoser, P. in *Compositional Data Analysis* 341–355 https://doi.org/10.1002/9781119976462.ch25 (John Wiley & Sons, 2011).
72. Koopmans, F. et al. SynGO: an evidence-based, expert-curated knowledge base for the synapse. *Neuron* **103**, 217–234 (2019).
73. Bates, D., Mächler, M., Bolker, B. & Walker, S. Fitting linear mixed-effects models using lme4. *J. Stat. Softw.* **67**, 1–48 (2015).
74. Love, M. I., Huber, W. & Anders, S. Moderated estimation of fold change and dispersion for RNA-seq data with DESeq2. *Genome Biol.* **15**, 550 (2014).
75. Yu, G., Wang, L.-G., Han, Y. & He, Q.-Y. clusterProfiler: an R package for comparing biological themes among gene clusters. *OMICS* **16**, 284–287 (2012).

Acknowledgements We thank J. R. Brown for input and assistance in editing the manuscript; N. Oliver, A. Altaf, L. L. Lyons, N. Kozub and S. Tropp for technical assistance; all of the members of the Arlotta laboratory for discussions; B. Cohen for the Mito210 iPS cell line; G. Church for the PGP1 iPS cell line; M. Talkowski (MGH) for the GM08330 iPS cell line; the staff at the Broad Genomics Platform for sequencing; M. Alawi for helping D.L. with the expansion microscopy analyses; and S. Rodriques and A. Payne for their contribution to early development of the epitope tag barcoding constructs.

Author contributions I.F. and N.A.-B. are equally contributing first authors; A.W. and T.F. are equally contributed second authors. N.A.-B., I.F. and P.A. conceived and designed the experiments. N.A.-B., I.F. and S.A. generated, cultured and characterized all of the organoids in this study, with the help of S.S.; P.A. supervised their work and contributed to data interpretation. N.A.-B. and I.F. worked on cell type assignments and scRNA-seq data analysis, and A.W. and T.F. performed all of the computational work under the supervision of A.R. and P.A.; A.S.K. performed methylome experiments and helped with analysis and interpretation. A.K. prepared the methylome libraries for sequencing. M.S. performed the computational analyses for the methylome data under the supervision of H.K. and A.M.; N.A.-B., I.F., S.A. and S.S. performed IHC and image acquisition. S.S. performed IHC and image acquisition and quantification related to SATB2 and FOS staining. A.S.K. performed NeuN IHC on long-term organoids. R.K. performed MEA recordings and S.M.Y. performed data analysis with the help of R.K.; M.M.C. performed all of the EM experiments and ground-truth analysis with the help of S.A. and Y.M.; Y.M. worked on the quantification algorithm for synapse quantification under the supervision of J.L.; N.A.-B. and I.F. performed scRNA-seq experiments with help from X.A. and supervision of P.A. and J.Z.L.; D.L. designed and performed the expansion microscopy epitope tag barcoding experiments and analyses, with help from E.Z., and B.A. contributed to early development of the epitope tag barcoding constructs, all under the supervision of E.S.B.; N.A.-B. and A.S.K. developed mouse endogenous chimeroids and performed the related experiments. N.A.-B. and I.F. performed scRNA-seq library preparation for the vast majority of the preparations included in this study. N.A.-B., I.F. and P.A. wrote the manuscript with contributions from all of the authors. All of the authors read and approved the final manuscript.

Funding This work was supported by grants from the Stanley Center for Psychiatric Research to P.A. and J.Z.L., the Broad Institute of MIT and Harvard, the National Institutes of Health (RF1MH123977 to P.A. and E.S.B.; R01MH112940 to P.A. and J.Z.L.; RF1MH132710 to J.L.; and R01AG087374, R01EB024261, R01AG070831 and RF1MH123403 to E.S.B.), the Blavatnik Biomedical Accelerator at Harvard University to P.A., the Klarman Cell Observatory to A.R., the Max Planck Society to A.M., and the HHMI, Lisa Yang, Schmidt Futures, Open Philanthropy/Good Ventures and John Doerr to E.S.B.

Competing interests P.A. is a scientific advisory board member at Foresite Labs, and is a co-founder of Vesalius and a co-founder and equity holder at Foresite Labs and at Avatar Bio. A.R. is a founder and equity holder of Celsius Therapeutics, an equity holder in Immunitas Therapeutics and, until 31 August 2020, was a scientific advisory board member of Syros Pharmaceuticals, Neogene Therapeutics, Asimov and Thermo Fisher Scientific. From 1 August 2020, A.R. has been an employee of Genentech and has equity in Roche. A.M. is a co-founder and scientific advisor of Harbinger Health, and is on the scientific advisory board of Zymo Research.

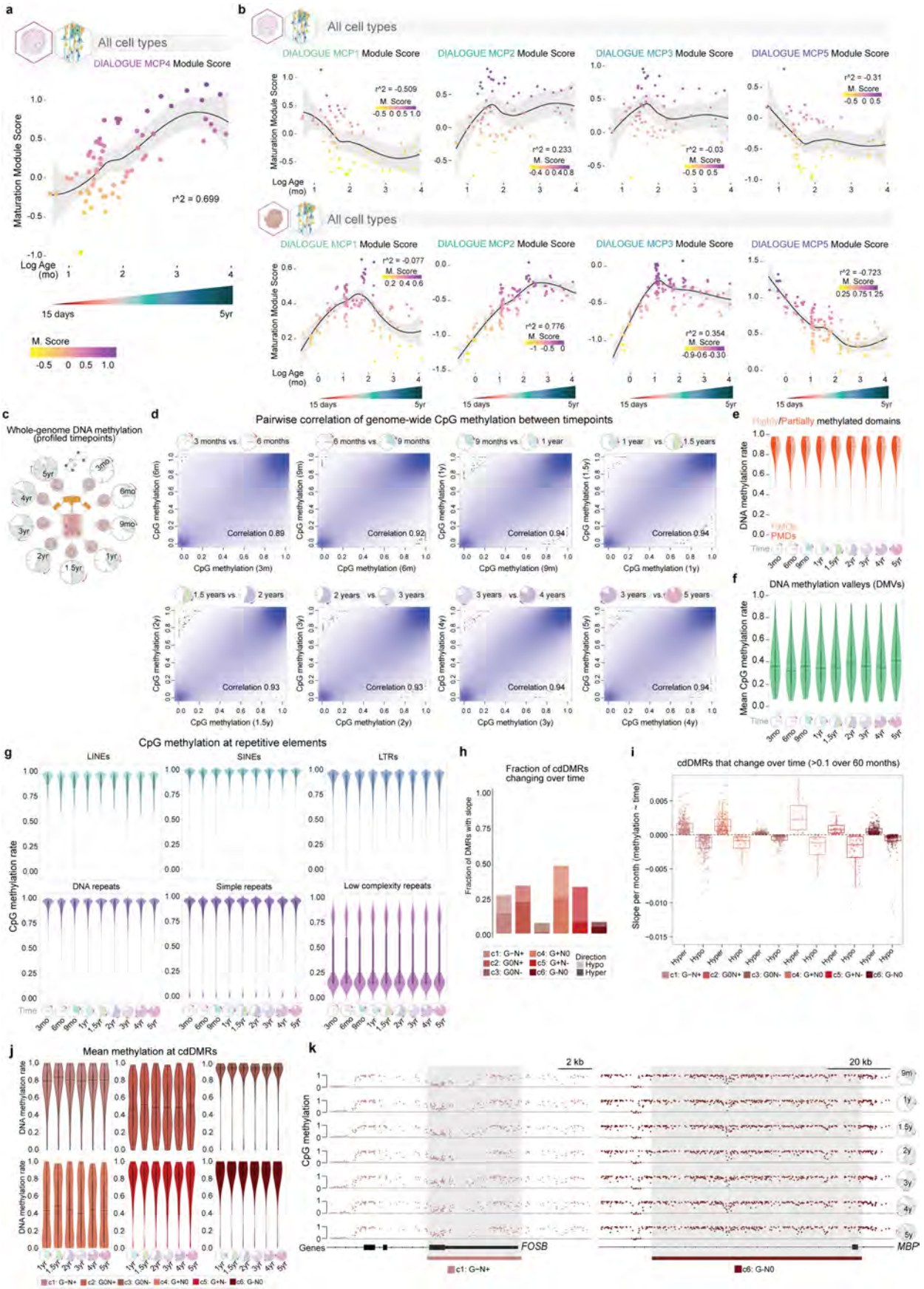
Additional information

Supplementary information The online version contains supplementary material available at https://doi.org/10.1038/s41586-026-10877-x.

Correspondence and requests for materials should be addressed to Paola Arlotta.

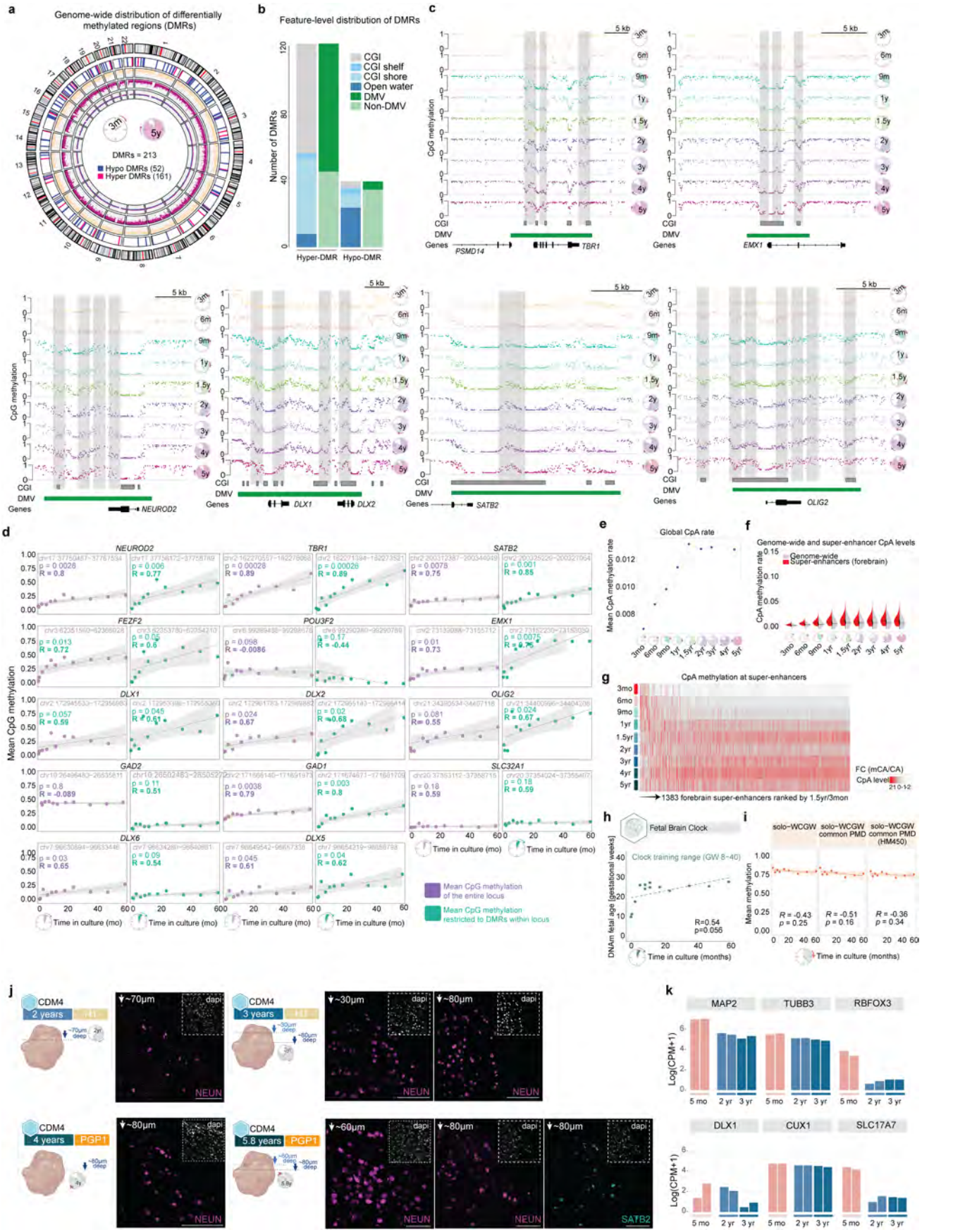
Peer review information *Nature* thanks Colette Dehay, Andrew Jaffe, Selene Lomoio and the other, anonymous, reviewer(s) for their contribution to the peer review of this work. Peer reviewer reports are available.

Reprints and permissions information is available at http://www.nature.com/reprints.



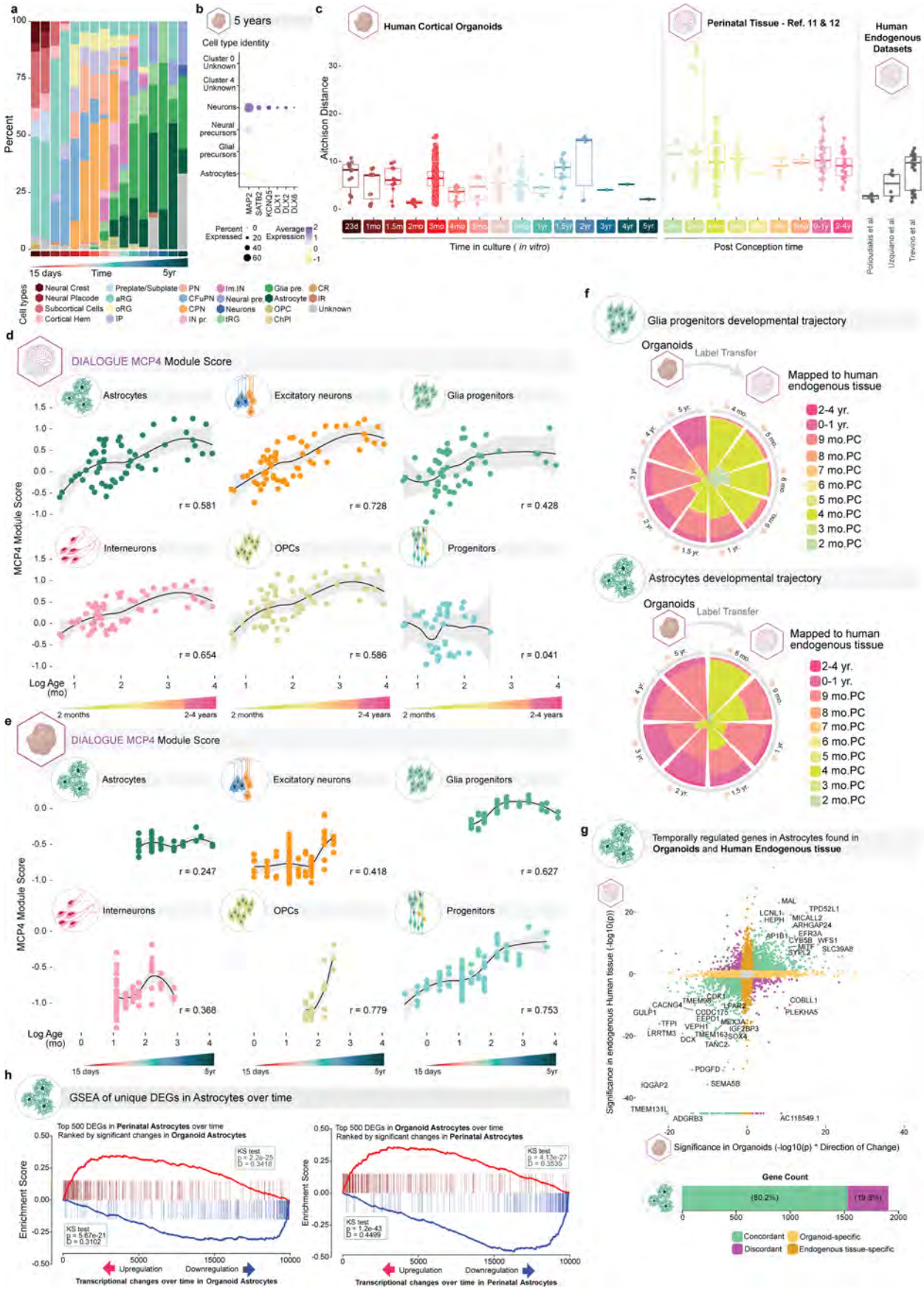
Extended Data Fig. 1 | See next page for caption.

Extended Data Fig. 1 | Longitudinal transcriptomic and epigenomic maturation of human brain organoids. a, Scatterplots showing the mean Maturation Score (DIALOGUE-MCP4) (y-axis) of all cells per donor along the developmental trajectory of endogenous human datasets (n = 62, 2mo PC to 4 years) grouped by timepoint (Log age in months, x-axis. Smoothed conditional means (black line) with default 95% confidence intervals (grey regions). Same plotting scheme as in Fig. 1e. **b**, Scatterplots showing the mean Maturation Score (DIALOGUE- from MCP1 to MCP5) in endogenous datasets (upper panels) and organoids (lower panels). Pearson's r values show correlation between age and Maturation scores. **c**, Overview of time points profiled by whole-genome bisulfite sequencing (WGBS). **d**, Pairwise density plots comparing genome-wide CpG methylation values between consecutive time points. Pearson correlation coefficients are indicated. Each dot is a single CpG. **e**, DNA methylation rates in highly and partially (HMD, PMD) methylated domains are shown. The line in the violin plot indicates the median of the distribution. (n = 16,445 PMDs; n = 10,552 HMDs). Boxplots parameters, see in **Methods-visualizations**. **f**, Distribution of average methylation levels within DMVs across time points. The line in the violin plot indicates the median of the distribution. (n = 1,152 DMVs). Boxplots parameters, see in **Methods-visualizations**. **g**, Distribution of average methylation levels across different repeat classes. (n = 303,843 LINEs; n = 849,490 SINEs; n = 208,712 LTRs; n = 69,719 DNA repeats; n = 1,552 low-complexity repeats). **h**, Mean DNA methylation at conserved developmental DMRS (cdDMRs). Violin plots show distribution of average CpG methylation at cdDMRs (defined from endogenous human cortex15) The horizontal line within each violin plot indicates the median methylation level. (n = 567, 423, 362, 96, 170, 560 cdDMRs in c1-c6, respectively; n = 2,178 cdDMRs in total). **i**, Fraction of cdDMRs changing over time. Barplots show the fraction of cdDMRs exhibiting methylation changes across organoid timepoints stratified by cluster (c1-c6). cdDMRs were classified based on linear regression slope across time: hypermethylated (slope > 0.1) or hypomethylated (slope < −0.1). Bars indicate the proportion of cdDMRs within clusters that meet these criteria. (n = 2,178 cdDMRs in total). **j**, Magnitude and direction of methylation change at dynamic cdDMRs. Boxplots display the distribution of regression slopes (methylation change per month) for cdDMRs with absolute slope > 0.1 over 60 months (5 years) in culture, separated into hyper- and hypomethylated groups and stratified by clusters (c1-c6). Individual points represent single cdDMRs. (hypermethylated: n = 331, 252, 163, 39, 75, 312 cdDMRs in c1-c6, respectively; hypomethylated: n = 236, 171, 199, 57, 95, 248 cdDMRs in c1-c6, respectively). Boxplots parameters, see in **Methods-visualizations**. **k**, Genome browser tracks of representative cdDMR loci, FOSB, and MBP. cdDMRs are highlighted (grey boxes). Genes are shown below. Scale bars indicate genomic distance. Some elements of the diagrams in **a** and **b** were created using BioRender; Antón-Bolaños, N. https://BioRender.com/9m183ab (2026).



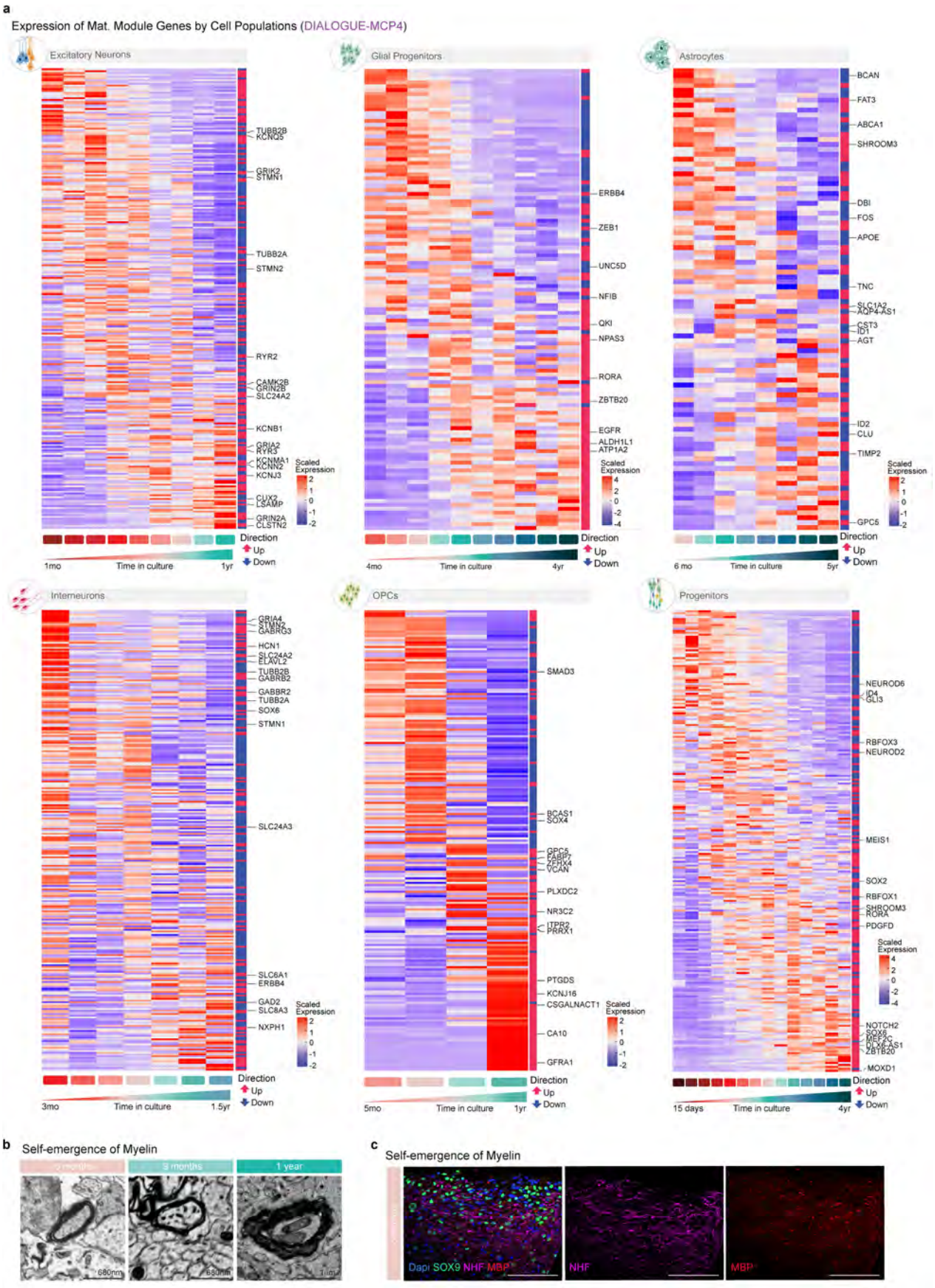
Extended Data Fig. 2 | See next page for caption.

Extended Data Fig. 2 | Longitudinal DNA methylation dynamics in aged organoids. a, Circus plot showing genomic positions of n = 213 DMRs (3-month and 5-year organoids, first inner track; red: hypermethylated, blue: hypomethylated). Outermost track shows the hg19 chromosome ideogram. Inner scatter tracks show genome-wide CpG methylation averaged in 50 kb bins for 3-month (second track) and 5-year (third track) organoids, followed by the difference in methylation (3 m – 5 y; innermost track). **b**, Genomic annotation of age-correlated DMRs, showing enrichment across CpG islands (CGIs) and DMVs. **c**, Genome browser tracks showing methylation profiles of DMRs at the TBR1, EMX1, NEUROD2, DLX1/2, SATB2, and OLIG2 loci across all time points. DMR regions are highlighted (grey boxes). CGIs, DMVs, and genes are annotated below. **d**, Scatterplot showing mean CpG methylation across time in culture for representative loci. For each gene, the mean methylation across the entire locus (magenta) and within the DMR (cyan) is plotted as a function of culture time (months). Each point represents one time point. Solid lines indicate linear regression fit with shaded areas representing 95% confidence intervals. Pearson correlation coefficients R and corresponding two-sided p-values are indicated in each panel. **f**, Distribution of average CpA methylation rates within forebrain super-enhancers and genome-wide 30 kb background bins. The line in the violin plot indicates the median of the distribution. (n = 1,379 super-enhancers; n = 93,061 background bins). **g**, Heatmap of the fold change of CpA methylation (1.5 yr/3 mo) at the forebrain super-enhancers. Column shows individual super-enhancers. **h**, Predicted DNA methylation age for the set of Fetal clock CpGs is presented. X-axis represents the chronological age of the organoids; y-axis predicted methylation age in the organoids. Dash line indicates perfect correlation and solid line linear regression with the R value. **i**, Scatterplot comparing time-in-culture (months) of sequenced organoids and average methylation rates at solo-WCGWs (left), solo-WCGWs in common PMDs (middle), and solo-WCGWs within common PMDs represented on the HM450 array (right). Red line: linear regression fit; Shaded area: 95% confidence intervals; R: Pearson correlation coefficient; p: two-sided correlation test p-value. **j**, NeuN immunohistochemistry of 2 and 3-year (top, n = 1 each) and 4 and 5.8-year (bottom, n = 2 and n = 1, respectively. Left panel SATB2 immunohistochemistry) CDM4 organoids. Scale bar: 100 µm. **k**, Barplot showing expression levels (y-axis; log-counts per million with added pseudocount) of excitatory and inhibitory neuronal markers in rRNA-depleted total bulk RNA-seq at 5 months, 2 and 3 years (n = 2 organoids each).



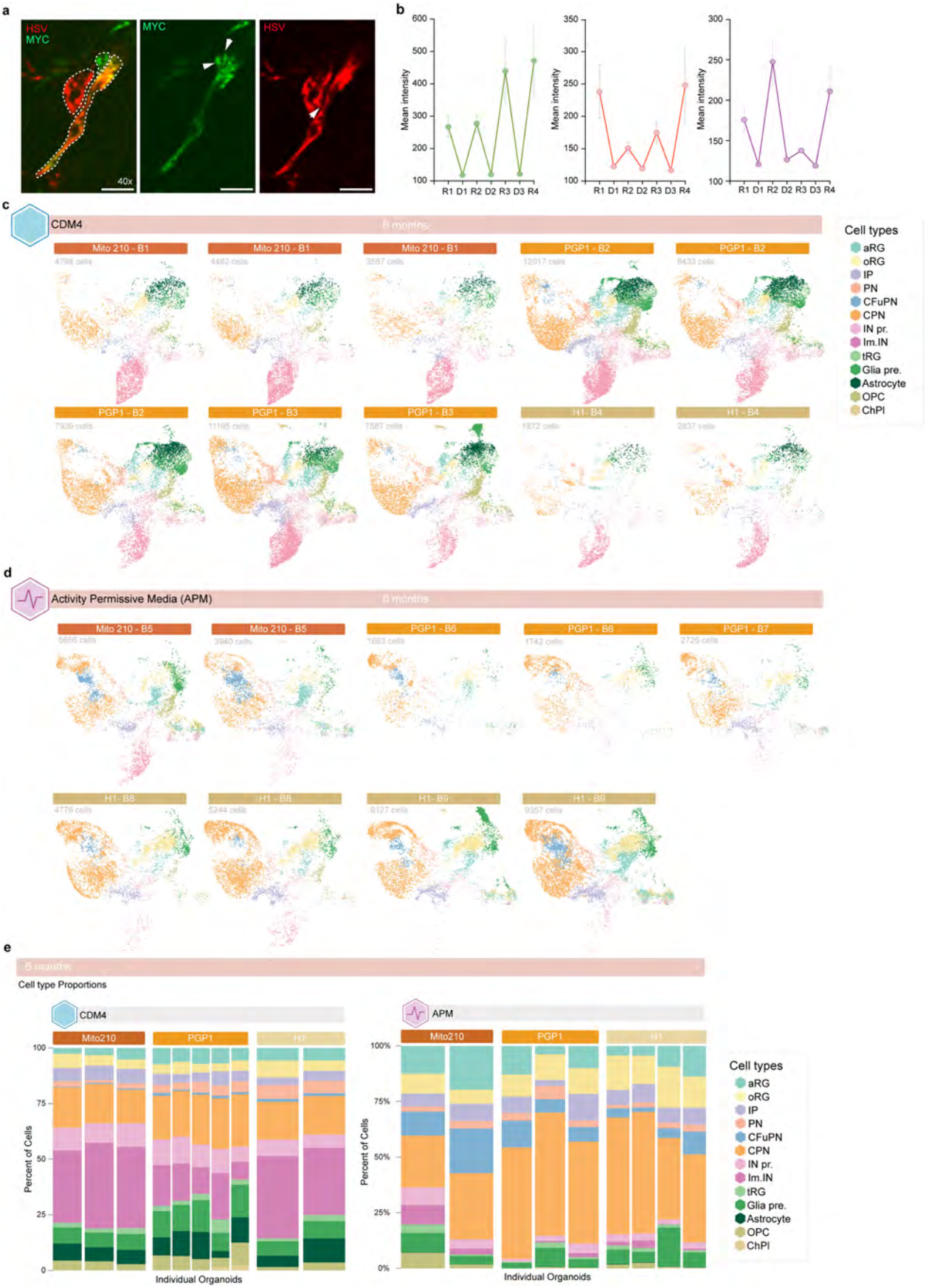
Extended Data Fig. 3 | See next page for caption.

Extended Data Fig. 3 | Organoid cell type dynamics and astrocyte maturation trajectories across extended culture. a, Stacked barplots showing cell-type abundance along organoid developmental trajectory (15 days to 5 years). **b**. Dotplot of percent of cells with nonzero expression (point size) and z-scaled average expression (point colour) of several neuronal marker genes (x-axis) within each cell type (y-axis) within 5.8-yo organoids. **c**, Boxplots showing the Aitchison distance between each pair of organoids within each timepoint (n = unique pairs from $C(r, 2)$, r represents the number of replicates per group on the x-axis; see Supplementary Table 1), and between pairs of endogenous human tissue samples from published datasets[6,10,11,38,39]. Boxes: median and IQR; whiskers: 1.5×IQR. **d-e**, Scatterplots showing the mean Maturation Score - MCP4 (y-axis) of astrocytes, excitatory neurons, and glial progenitors, interneurons, OPCs and progenitors within each endogenous tissue sample (d) and each organoid sample (e), grouped by timepoint (x-axis) (see Methods for plotting scheme). **f**, Rose plots showing endogenous human tissue age range[10] (2 months post conception (PC) to 4 years) of glia progenitors (upper) and astrocytes (lower) mapped from each organoid timepoint by label transfer. **g**, Scatterplot showing temporally regulated genes in astrocytes in organoids (x-axis) and endogenous human tissue (y-axis). Values are the product of $-\log_{10}(P) \times \mathrm{sgn}(\log_2 FC)$ of a temporal DEG. Colours indicate genes significantly regulated in the same direction in organoids and tissue (teal, 1530 genes), opposite directions (magenta, 377 genes), only in organoids (light yellow, 3535 genes), only in tissue (dark yellow, 2551 genes), or not significant in either (grey, 6946 genes). The stacked barplot summarizes the % of concordant (green) and discordant (magenta) significant temporal DEGs in astrocytes between organoids and tissue. **h**, Gene set enrichment analyses comparing temporal changes in organoid astrocytes to temporal changes in endogenous perinatal human cortex[10,11]. D-statistic and P-values derived from one-sided KS tests shown in boxed text (see Methods). Some elements of the diagrams in **d**–**h** were created using BioRender; Antón-Bolaños, N. https://BioRender.com/9m183ab (2026).



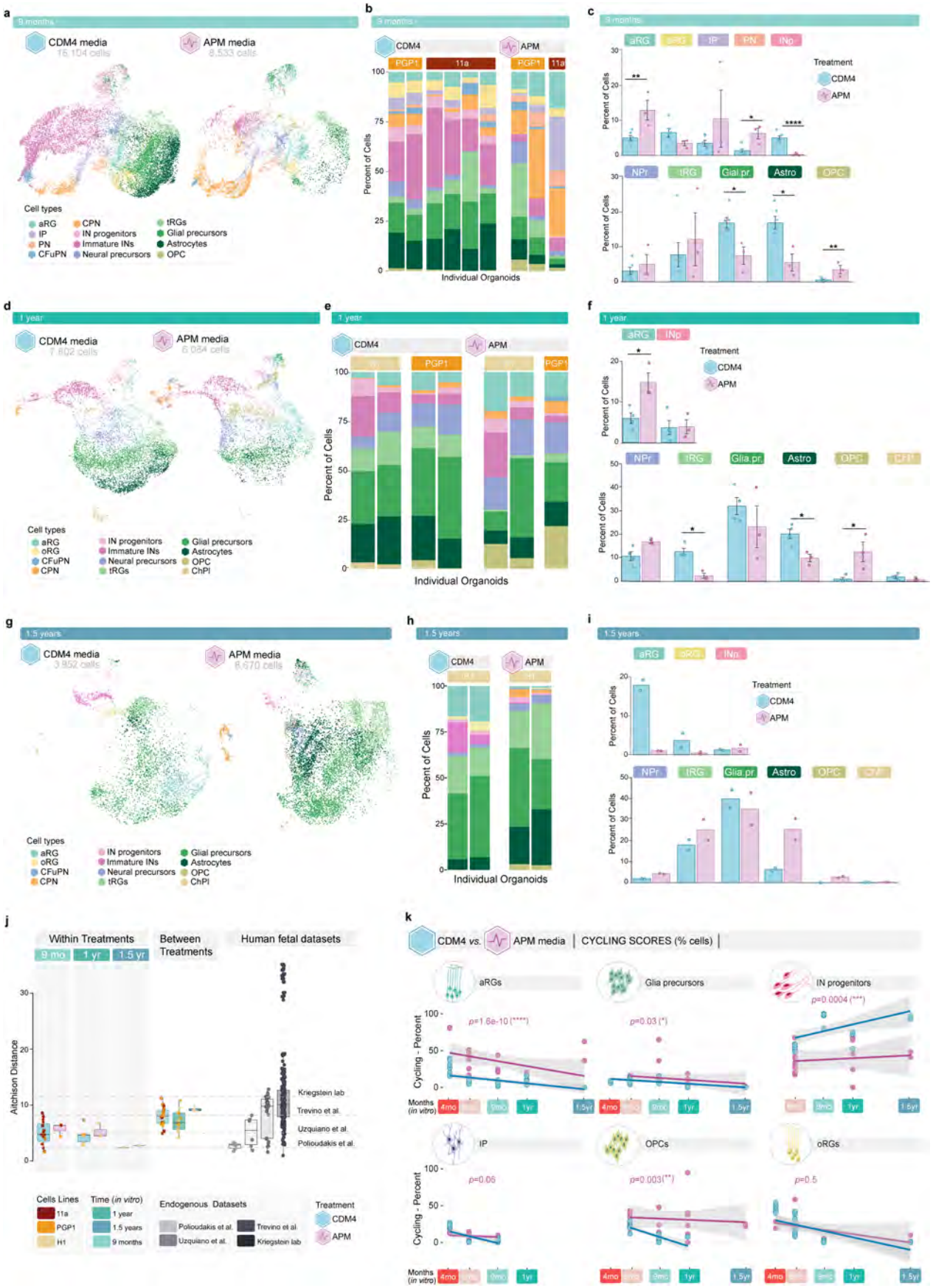
Extended Data Fig. 4 | See next page for caption.

Extended Data Fig. 4 | Long-term organoid maturation is associated with MCP4 transcriptional progression. a, Heatmaps showing the expression of all genes contributing to DIALOGUE's MCP4 within a given cell population in organoids across time. Values for each timepoint represent the mean of the counts-per-million of the pseudobulked count matrices for that cell type within each organoid within that timepoint, Z-scored for each gene. Genes are ordered by the weighted expression over time; genes expressed mostly at earlier time points are at the top, and genes expressed mostly at later time points are at the bottom. The colour bar on the right indicates whether the gene was marked as in the "up" (red) or "down" (blue) aspect of MCP4. Labelled genes were manually selected to show important biological features over time. **b**, Electron microscopy representative images showing the presence of myelin along the longitudinal trajectory; 6 months (n = 3 organoids), 9 months (n = 1), and 1 year (n = 6). **c**, Immunohistochemistry of organoids at 6 months showing the presence of myelinated axons, total n = 4 organoids (n = 2 for each of H1 and 11a cell lines). Scale bar: 100 µm. Some elements of the diagrams in **a** were created using BioRender; Antón-Bolaños, N. https://BioRender.com/9m183ab (2026).



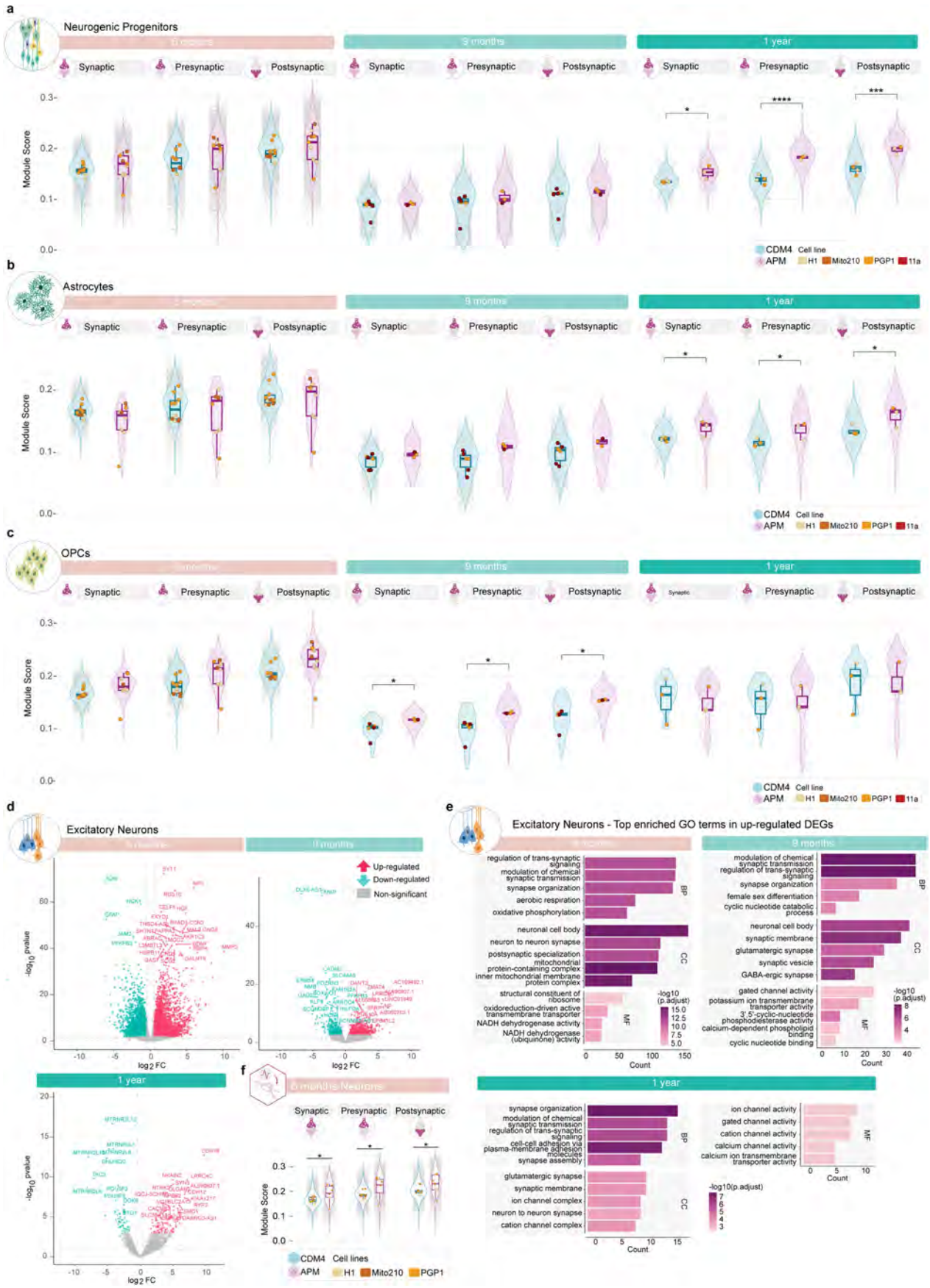
Extended Data Fig. 5 | See next page for caption.

Extended Data Fig. 5 | Single-cell profiling of 6-month organoids cultured in CDM4 and APM across batches and genetic backgrounds. a, Expression of different cytosolic epitope tag combinations enables tracing of densely packed neuronal processes, visualized here with two representative epitope tags. Three processes expressing either Myc tag, HSV tag, or both can be seen (indicated by dashed white lines). While expression of Myc tag or HSV tag alone would not allow unambiguous separation of these processes (see white arrows), combinatorial epitope tag expression enables their identification as three distinct neuronal processes. n = 3 organoids/treatment (APM, CDM4) and n = 10 neurons/organoid. Scale bar: 10 µm. **b**, Quantification of antibody de-staining efficiency in the three imaged colour channels. R1-4 = staining rounds. D1-4 = de-staining rounds. **c**, UMAP of 6-month CDM4-treated organoids, split by organoid and coloured by cell types. **d**. UMAP of 6-month APM-treated organoids, split by organoid and coloured by cell types. **e**, Stacked barplots showing the cell type compositions of each 6-month CDM4- and APM-treated organoid, subgrouped by genetic background/cell line.



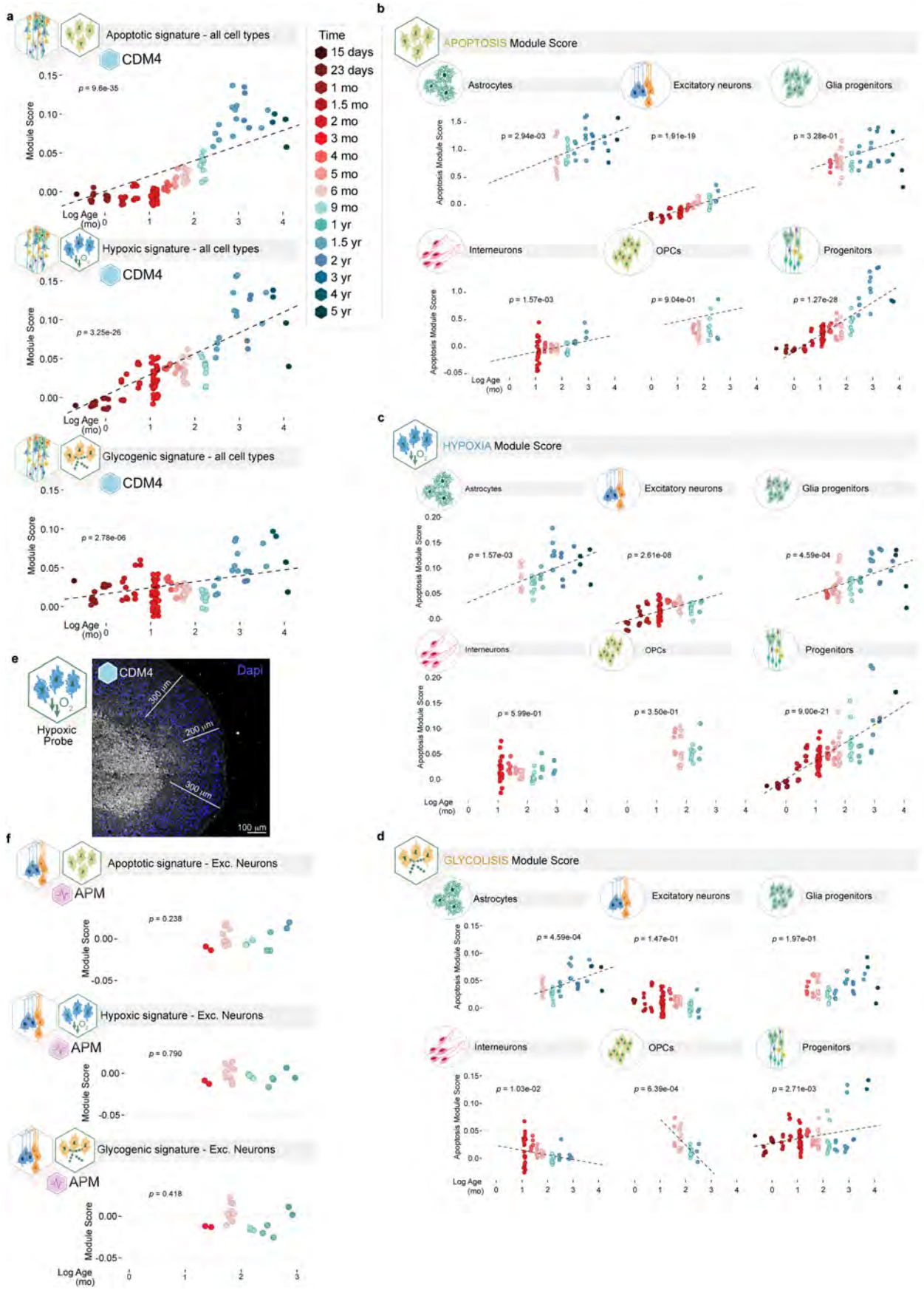
Extended Data Fig. 6 | See next page for caption.

Extended Data Fig. 6 | Longitudinal single-cell analysis identifies treatment-dependent changes in cell composition in long-term organoids. a, UMAP of integrated scRNA-seq data from 9-month CDM4- (n = 18,104 cells/6 organoids) and APM-treated (n = 8533 cells/3 organoids), coloured by cell types. **b**, Stacked barplots showing cell type compositions (9-month) grouped by treatment and subgrouped by cell line. **c**, Changes of cell type proportions between CDM4- (n = 6) and APM-treated (n = 3) organoids at 9 months. Bars: mean percentage of cell types; error bars indicating ± SEM. FDR-adjusted *P*-values derived from one-sided Likelihood Ratio Test and denoted by $^{*}P < 0.05$; $^{**}P < 0.01$; $^{***}P < 0.001$; $^{****}P < 0.0001$ (see Methods and Supplementary Table 7). **d**, UMAP of integrated scRNA-seq data from 12-month CDM4- (n = 7802 cells/4 organoids) and APM-treated (n = 6084 cells/3 organoids) organoids, coloured by cell types. **e-f**, Same methods and plotting scheme as in **b-c** for 1-year organoids. **g**, UMAP of integrated scRNA-seq data from 1.5-year CDM4- (n = 3,952 cells/2 organoids) and APM-treated (n = 8,670 cells/2 organoids) organoids, coloured by cell types. **h-i**, Same analysis and plotting scheme as in **b-c** for 1.5-year organoids. **j**, Aitchison distance measuring the differences in cell type compositions were calculated for unique pairs of samples within/between treatment conditions at 9-mo, 1 and 1.5 years. For each age, Aitchison distances between replicates within each treatment were compared by the two-sided Wilcoxon rank-sum test, and no significant dis-similarity was shown (4mo: $P = 0.375$, n = 15 CDM4/1 APM; 9mo: $P = 0.738$, n = 15 CDM4/3 APM; 1 yr: $P = 0.714$, 6 CDM4/3 APM; 1.5 yr: P = NA, n = 1 CDM4/1 APM; n = unique pairs of replicates per group on the x-axis; see Supplementary Table 1). Boxes: median and IQR; whiskers: 1.5×IQR. Dotted lines: means for Aitchison distances for endogenous human fetal cortex datasets. **k**, Scatterplots showing the percentage of progenitor cells within each organoid that are cycling (y-axis) by organoid age (x-axis). Black lines: smoothed conditional means; grey regions: 95% CIs. FDR-adjusted *P* values are derived from one-sided likelihood ratio comparing binomial mixed-effects models, with 'organoid' as a random effect, with and without treatment as a covariate, denoted by $^{*}P < 0.05$; $^{**}P < 0.01$; $^{***}P < 0.001$; $^{****}P < 0.0001$. Some elements of the diagrams in **k** were created using BioRender; Antón-Bolaños, N. https://BioRender.com/9m183ab (2026).



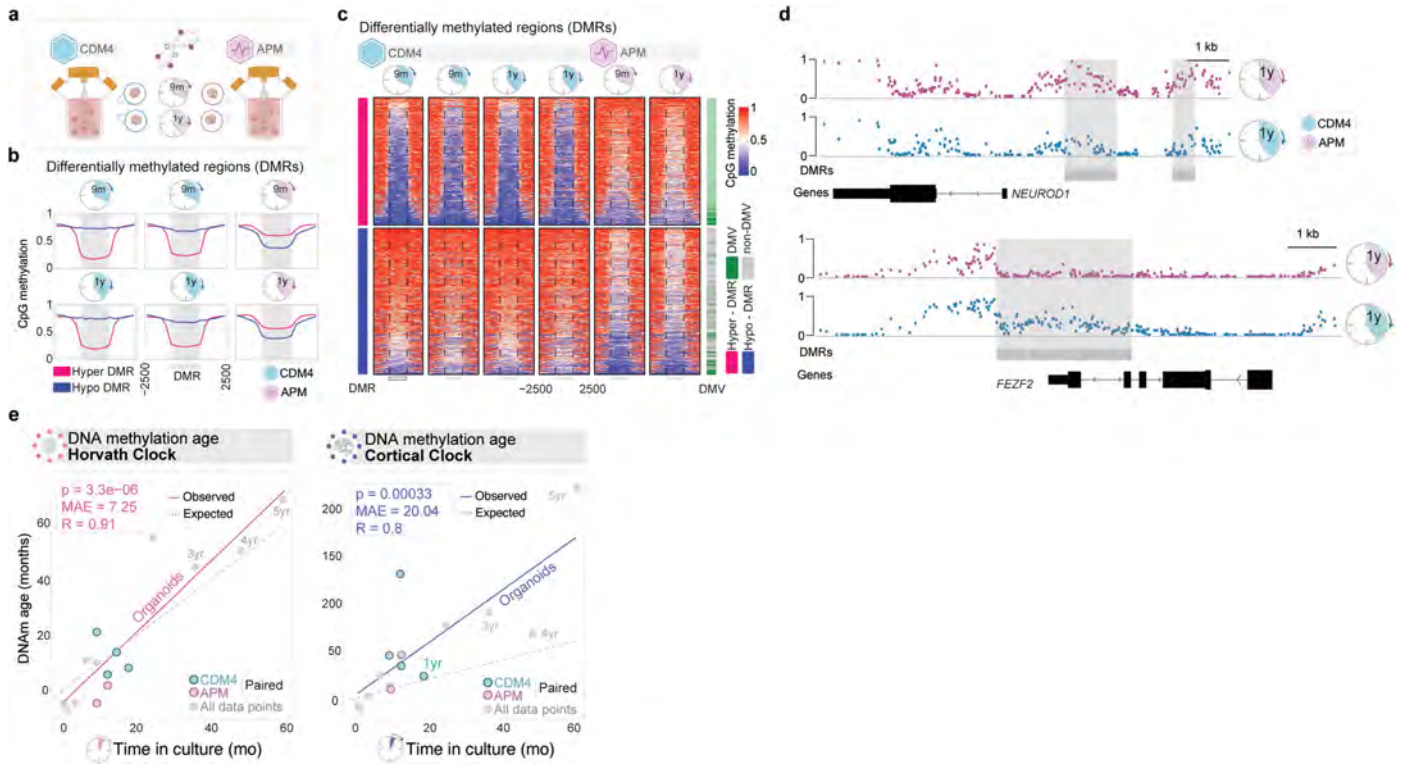
Extended Data Fig. 7 | See next page for caption.

Extended Data Fig. 7 | APM treated organoids show increased expression of synaptic genes and neuronal maturation signatures. a-c. Expression of three SynGO synaptic genes sets in different cell populations from CDM4- and APM-treated organoids at 6 months (CDM4: n = 10 organoids; APM: n = 9 organoids), 9 months (CDM4: n = 6; APM: n = 3), and 12 months (CDM4: n = 4; APM: n = 3). Neurogenic progenitors include aRGs, oRGs, tRGs, IPs, and IN progenitors. Module scores were calculated by Seurat's AddModuleScore function using presynapse (GO:0098793), and postsynapse (GO:0098794) gene sets. Grey dots: denoting cell-level scores with violins describing distributions. Coloured dots: averaged scores within given cell populations by organoids. Boxes (organoid-level): median and IQR; whiskers: 1.5×IQR. Differences between CDM4- and APM-treated organoids in each population at each age are are derived using one-sided likelihood ratio test comparing linear mixed-effects models, denoted by $^{*}P < 0.05$; $^{**}P < 0.01$; $^{***}P < 0.001$; $^{****}P < 0.0001$ (Supplementary Table 9). **d**, Pseudobulked differential expression analysis of comparing excitatory neurons between CDM4- and APM-treated organoids at 6, 9, and 12 months. Volcano plots display the differentially expressed genes (DEGs) based on significance cutoffs (Dashed lines: |Log2 Fold Change | > 0.5 and FDR-adjusted *P*-value < 0.05). The top 30 DEGs with the highest significance are labelled. **e**, Top 5 enriched Gene Ontology (GO) terms per ontology category of up-regulated DEGs in excitatory neurons of APM-treated organoids at 6, 9, and 12 months (see Methods). **f**, Expression of three SynGO synaptic gene sets is higher in neurons of APM-treated organoids at 6 months (CDM4: 29,987 cells, n = 10 organoids; APM: 22,422 cells, n = 9 organoids). Same analysis and plotting scheme as in **a-c** (Supplementary Table 8). Some elements of the diagrams in **a-f** were created using BioRender; Antón-Bolaños, N. https://BioRender.com/9m183ab (2026).

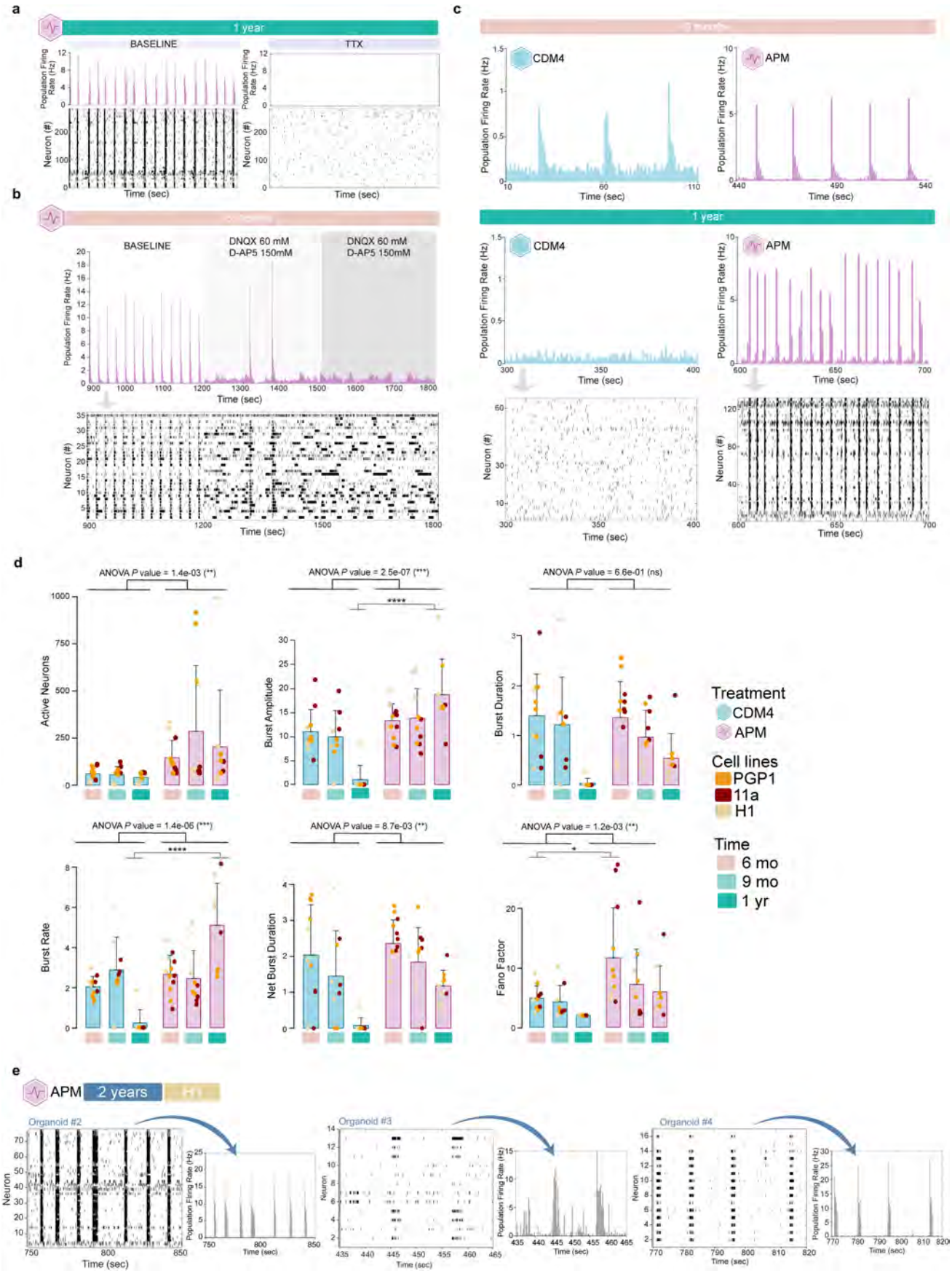


Extended Data Fig. 8 | See next page for caption.

Extended Data Fig. 8 | Metabolic stress-associated transcriptional programs emerge during organoid culture but are attenuated in APM excitatory neurons. a, Scatterplots showing mean module scores (y-axis) for MSigDB's Hallmark gene sets for apoptosis (top), hypoxia (middle), and glycolysis (bottom) across time (x-axis; log months in vitro) in cortical organoids (n = 110 organoids, 424,720 cells). Trendlines and P-values come from mixed-effects models with log-age as a continuous fixed effect, and with organoid and broad cell type as random effects (one-sided likelihood ratio test). Points show mean values per organoid, but statistics were calculated based on single-cell data. **b-d**, Same as a, but with data split by broad cell type. Consequently, P-values and trendlines derive from models that do not include broad cell type as a covariate but otherwise are as described above. Trendlines are only drawn in cases where there is significant ($P < 0.05$) change over time. **e**, Immunohistochemistry of a 1-year-old CDM4 organoid (n = 3) with Hypoxyprobe showing the metabolically challenged centre of the organoid. **f**, Scatterplots showing mean module scores (y-axis) for MSigDB's Hallmark gene sets for apoptosis (top), hypoxia (middle), and glycolysis (bottom) across time (x-axis, log months) in excitatory neurons within APM-treated cortical organoids (n = 19 organoids, 27,657 cells). Mixed-effects models with log-age as a continuous fixed effect and organoid as a random effect did not show any significant change in module scores over time (P-values shown in panel, one-sided likelihood ratio test). Some elements of the diagrams in **a**-**d** were created using BioRender; Antón-Bolaños, N. https://BioRender.com/9m183ab (2026).

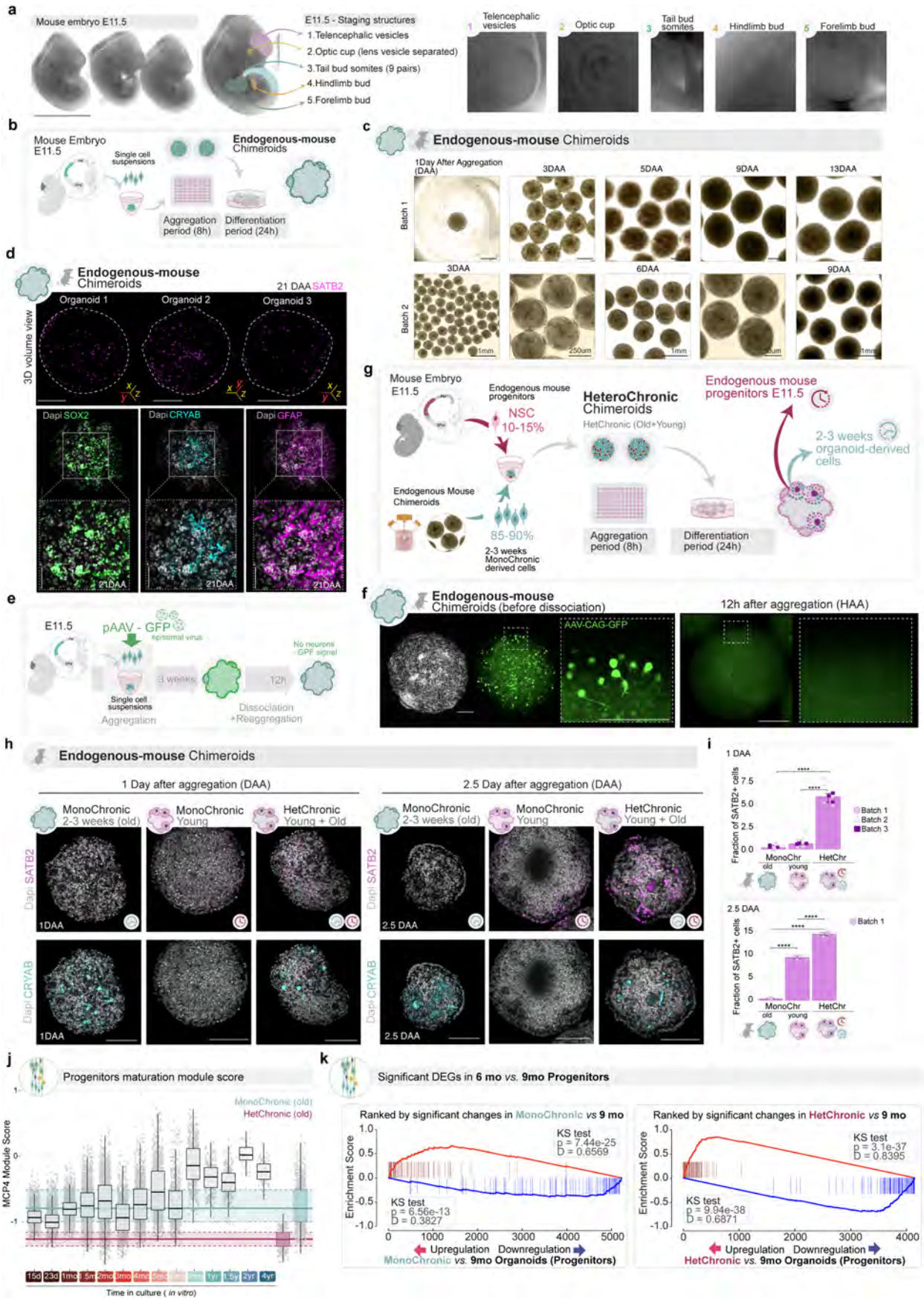


Extended Data Fig. 9 | WGBS reveals differential methylation landscapes between CDM4- and APM-treated long-term organoids. a, Experimental overview of cortical organoids generated under two culture conditions (CDM4 and APM) and profiled by WGBS at 9 months and 1 year. **b**, Differentially methylated regions (DMRs) between culture conditions. Average CpG methylation profile across hyper- and hypomethylated DMRs identified at 9 months and 1 year. The dashed line denotes the DMR, and flanking regions represent +/− 2.5 kb. **c**, Heatmap showing CpG methylation profiles of DMRs across both profiled time points between the conditions. DMRs are grouped into hyper-and hypomethylated clusters. Overlaps with DNA methylation valleys (DMVs) are indicated on the right. **d**, Genome browser views showing CpG methylation profiles at the NEUDO1 and FEZF2 loci in CDM4 and APM organoids at 1 year. DMR regions are highlighted (grey boxes). Scale bars indicate genomic distance. **e**, The predicted DN methylation age using the Horvath clock (left) and cortical clock (right) CpG sets is shown. The x-axis represents chronological age of the organoids (months in culture), and the y-axis represents predicted DNA methylation age (months). The dashed line indicates perfect correlation, and the solid line represents the linear regression fit; shaded area: 95% confidence intervals; Pearson correlation coefficient R, p: two-sided correlation test p-value. MAE indicates the mean absolute error.



Extended Data Fig. 10 | See next page for caption.

Extended Data Fig. 10 | Longitudinal comparison of network activity in CDM4 and APM organoids. a, Tetrodotoxin (TTX) abolished the spiking activity. Example recording is presented through the population-averaged firing rate (top) and a spike raster plot from all detected units (bottom). **b**, Network bursts are mediated by glutamatergic neurotransmission. Population firing rate and spike raster plot of a representative organoid treated with glutamate receptor antagonists (DNQX and D-AP5). **c**, Representative population-averaged firing rate and spike raster plot for a subset of units in 6-month (top) and 12-month (bottom) organoids, showing the difference between CDM4 (left) and APM (right) groups. **d**, Characterization of the network bursting activity for CDM4- and APM-treated organoids. For metric FanoFactor, two outliers were removed based on the ROUT method (see Methods). For each measured metric by MEA, a Type III two-way ANOVA test was performed to assess the effects of Treatment, Age, and their interaction Treatment:Age (n = samples for CDM4 vs. APM; 6 months: 11 vs. 13; 9 months: 9 vs. 10; 1 year: 8 vs. 9. For cases where quantifications of more than one cell line were available, the genetic background was included as a fixed effect. ANOVA *P* value is shown to denote the significance of the Treatment effect on the measured metric, as represented by asterisks. Bars: the mean of measured values; error bars indicate + SD. Post-hoc Tukey tests were performed to determine at which age the treatment significantly differ and adjusted *P* values by Tukey's HSD method were represented by asterisks. **e**, Raster plots of 2-year APM organoids (n = 3).



Extended Data Fig. 11 | See next page for caption.

Extended Data Fig. 11 | Heterochronic chimeroids shift old progenitors toward younger-like neural states. a, Representative staged E11.5 embryos with annotated structures (n > 60 embryos, 6 batches). Scale bar 1 mm. **b**, Schematics of endogenous mouse chimeroids (n = 384 chimeroids, 4 batches). **c**, Brightfield images of endogenous chimeroids after dissociation. DAA, days after aggregation. Scale 100µm (top) and 1 mm (bottom-zoom out), and 250µm (bottom-zoom in), n = 3. **d**, Whole-mount immunofluorescence (WMIF) of endogenous chimeroids 2-3 weeks after aggregation. 3D volume view of SATB2 immunostaining (top). Dotted lines denote individual organoids. x,y,z denote the angle of rotation. The scale 500µm. Zoom-out and zoom-in view of the organoids stained with SOX2, CRYAB, GFAP (bottom), n = 3 organoids). The scale 100µm. **e**, Schematics of the generation of GFP^+ endogenous chimeroids utilizing AAV-GFP transduction and generation of MonoChronic (Old) mouse chimeroids. **f**, GFP^+ endogenous chimeroids before dissociation (left); 12 h after aggregation MonoChronic (Old) mouse chimeroids do not contain GFP^+ cells. n = 3 organoids. Scale bar 500µm. **g**, Schematics of HeteroChronic (Old + Young) mouse chimeroids. **h**, WMIF of SATB2 and CRYAB, 1 and 2.5 day after aggregation. Single *z*-stack is shown (n = 3 organoids per condition and timepoint). Scale bar is 100µm. **i**, Quantification of SATB2 signal. Bar plot showing the proportions of $SATB2^+$ nuclei, grouped by MonoChronic (Old), MonoChronic (Young), and HeteroChronic (Old +Young) from cultures 1 days (D1AA; for each group: n = 9 organoids from 3 batches) and 2.5 days (D2.5AM; for each group: n = 3 organoids from one batch) after aggregation. Bars: mean values with error bars indicating ± SEM. Jittered dots: quantification of each sample, are shaped and coloured by batches. The significance of the condition effect on proportional differences across three groups at D1AM was indicated by ANOVA $P = 6.15 \times 10^{-17}$, derived from one-sided likelihood ratio test). Two-sided Tukey-adjusted *P*-values for pairwise comparisons between groups were represented by asterisks. (MonoChronic-old vs HeteroChronic: $P = 2.35 \times 10^{-14}$; MonoChronic-young vs HeteroChronic: $P = 2.49 \times 10^{-14}$; MonoChronic-old vs MonoChronic-young: $P = 0.17$; see Methods). **j**, MCP4 maturation module score (y-axis) in progenitors cells of the old portion of HeteroChronic (n = 822 cells) and 9-month MonoChronic (n = 10,610 cells) chimeroids, compared to progenitors in a cortical organoid timeseries (15 days to 4 years, n = 123,125 cells) (x-axis; timepoint). Grey boxes show median and 1st and 3rd quartiles, with whiskers showing 1.5 interquartile ranges for each organoid timepoint. Solid lines represent median MCP4 scores for HeteroChronic (magenta) and MonoChronic (teal), with dashed-line bounded shaded areas representing upper and lower quartiles. **k**, Gene set enrichment analysis (GSEA) plot. Significantly differentially expressed genes were identified between 6mo and 9mo organoid progenitor cells using DESeq2. These genes were split into two groups: genes upregulated in 6mo organoids (red), and genes downregulated in 6mo organoids (blue). These genes were used as input for Kolmogrov-Smirnov (KS) tests against a ranked list of genes based on DE analyses between MonoChronic Chimeroids vs 9mo organoids (top) and between HeteroChronic Chimeroids vs 9mo organoids (bottom). Red and blue curves represent running Enrichment Scores for each test, with maximum absolute values of each Enrichment Score listed as the KS test D-statistic. High significance indicates that both MonoChronic and HeteroChronic progenitors differ from 9mo progenitors in a direction similar to 6mo progenitors, with HeteroChronic showing stronger enrichment toward younger organoid states. Some elements of the diagrams in **j** and **k** were created using BioRender; Antón-Bolaños, N. https://BioRender.com/9m183ab (2026).